

Growth mode and frictional properties of ultrathin
films of sodium chloride on copper surfaces

Patrick Delage
Department of Physics
McGill University
Montreal, Québec
CANADA

October 3, 2005

A thesis submitted to the
Faculty of Graduate Studies and Research
in partial fulfillment of the requirements
for the degree of Master of Science

© Delage, 2005



Library and
Archives Canada

Bibliothèque et
Archives Canada

Published Heritage
Branch

Direction du
Patrimoine de l'édition

395 Wellington Street
Ottawa ON K1A 0N4
Canada

395, rue Wellington
Ottawa ON K1A 0N4
Canada

Your file *Votre référence*
ISBN: 978-0-494-22714-5
Our file *Notre référence*
ISBN: 978-0-494-22714-5

NOTICE:

The author has granted a non-exclusive license allowing Library and Archives Canada to reproduce, publish, archive, preserve, conserve, communicate to the public by telecommunication or on the Internet, loan, distribute and sell theses worldwide, for commercial or non-commercial purposes, in microform, paper, electronic and/or any other formats.

The author retains copyright ownership and moral rights in this thesis. Neither the thesis nor substantial extracts from it may be printed or otherwise reproduced without the author's permission.

AVIS:

L'auteur a accordé une licence non exclusive permettant à la Bibliothèque et Archives Canada de reproduire, publier, archiver, sauvegarder, conserver, transmettre au public par télécommunication ou par l'Internet, prêter, distribuer et vendre des thèses partout dans le monde, à des fins commerciales ou autres, sur support microforme, papier, électronique et/ou autres formats.

L'auteur conserve la propriété du droit d'auteur et des droits moraux qui protègent cette thèse. Ni la thèse ni des extraits substantiels de celle-ci ne doivent être imprimés ou autrement reproduits sans son autorisation.

In compliance with the Canadian Privacy Act some supporting forms may have been removed from this thesis.

Conformément à la loi canadienne sur la protection de la vie privée, quelques formulaires secondaires ont été enlevés de cette thèse.

While these forms may be included in the document page count, their removal does not represent any loss of content from the thesis.

Bien que ces formulaires aient inclus dans la pagination, il n'y aura aucun contenu manquant.


Canada

Abstract

The epitaxial growth of ultrathin films of NaCl was achieved on a Cu(100) substrate at room temperature. The growth mode was observed to be of the Stranski-Krastanov type using non-contact AFM, with well-oriented square islands growing on top of the first monolayer of NaCl. The frictional properties of different monolayers were measured using contact mode AFM. The friction contrast between the different monolayers of NaCl was found to be too small to be measured within the noise. Atomic stick-slip measurements were performed on a NaCl island. The results are discussed in comparison with relevant literature on thin films of alkali halides.

Résumé

La croissance épitaxiale de couches ultra-minces de NaCl a été réalisée sur un substrat de Cu(100) à température ambiante. La croissance observé est de type Stranski-Krastanov en utilisant un AFM de type non contact, avec les îles carrées bien orientées se formant sur la première monocouche du NaCl. Les propriétés de friction de différentes monocouches ont été mesurées en utilisant un AFM en mode contact. Le contraste de frottement entre les différentes monocouches du NaCl s'est avéré trop petit pour être discerné du bruit. Des mesures de type "stick-slips" ont été exécutés sur une île de NaCl. Les résultats sont discutés en comparaison avec la littérature pertinente sur les couches minces des halogénures d'alcali.

Acknowledgments

First of all, I want to thank my supervisor, Roland Bennewitz, for giving me the opportunity to pursue my studies at a graduate level at McGill University. Thank you very much for all the help and the advices you provided me, and thank you for providing me the much needed motivation when I needed it. I also want to thank my other research group members, Tobin Filleter, Sabine Maier and Jonathan David, for helping me on various aspects in my project. Without you this project would have been a lot lengthier and harder! A great thanks to Steve Kecani and Eddie Del Campo at the machine shop for the time they have spent helping me, and especially for teaching me great skills. I also want to thank Robert Gagnon for showing me a lot of sample preparation techniques and other useful skills. Thanks to Michel Beauchamp and Steve Godbout for their help with the various requests I've made.

I really want to take my family for the much needed support they provided me during this project. Merci pour tout! A special thanks goes to all my friends who have suffered my constant complaining over nothing, and never stop believing in me, and also my roommates, who have never stopped motivating me. Merci Jean-Philippe, merci de m'avoir encouragé, supporté et surtout enduré, jusqu'à la toute fin. MERCI

Carl-Eric et Rémi, les mots me manquent... Vous avez été présent tout au long de cette aventure, m'encourageant quand il le fallait, me relevant même parfois. Sans vous, ceci n'aurait jamais vu le jour et je vous remercie d'avoir cru en moi jusqu'au bout.

Contents

1	Introduction	1
1.1	History and origin of tribology	1
1.2	Friction at the nanoscale	3
1.3	Nanotribology	4
2	Instrumentation	5
2.1	Surface science methods	5
2.1.1	Ultrahigh vacuum	5
2.1.2	Sample preparation	9
2.1.3	Low energy electron diffraction	10
2.1.4	Auger electron spectroscopy	12
2.1.5	Scanning probe microscopy and other imaging techniques . . .	18
2.2	Ultrahigh vacuum system	24
2.3	Scanning force/tunneling microscope	24
2.4	Copper sample	25
2.4.1	Sample holder	26
2.4.2	Preparation of the copper surface	28
2.4.3	Characterization of the copper surface	28
2.5	Homebuilt evaporator	30
2.5.1	Characteristics	31
2.5.2	Design and fabrication	31
2.5.3	Testing and calibration of the evaporator	34

<i>CONTENTS</i>	iii
3 Experiments	37
3.1 Growth modes	37
3.1.1 Interfacial energies	37
3.1.2 Reflectivity of lattice steps	40
3.2 Growth mode of ultrathin films of NaCl on Cu(100)	42
3.2.1 Non-contact AFM topography of NaCl on Cu(100)	42
3.2.2 Stranski-Krastanov growth mode	44
3.2.3 Shape and orientation of the NaCl islands	46
3.2.4 Steps on a fcc metal and Smoluchowski effect	49
3.2.5 The edge of the salt film	51
3.3 Comparison with literature	51
4 Friction on NaCl/Cu(100)	58
4.1 Contact AFM measurements on NaCl-Cu(100)	59
4.2 Difficulties to image two materials in contact mode	61
4.3 Friction contrast	62
4.4 Stick-slip over a NaCl island	65
4.5 Comparison with literature	67
5 Conclusion	71
A UHV System	73
B Auger Electron Spectroscopy	74
C Evaporator	75

List of Figures

2.1	Operating pressure range for different types of pumps	7
2.2	Schematic diagram of a noble gas ions sputter gun	9
2.3	A schematic design of a standard four-grid LEED set-up with a typical LEED pattern exposing a Si(111)7 × 7 surface	11
2.4	Auger emission processes	13
2.5	Schematic representation of an Auger set-up	14
2.6	AES thin films	16
2.7	Schematic diagram of an STM along with its operating modes	19
2.8	Schematic diagram of an AFM along with its operating modes	21
2.9	Schematic representation of the copper sample	25
2.10	Construction of the copper sample holder	27
2.11	Typical LEED image of the copper surface	28
2.12	A typical AES spectrum of the copper sample	29
2.13	Typical STM images of the copper surface	30
2.14	Three different parts used to build the evaporator	32
2.15	The multiple flange adapter and the groove grabbers	33
2.16	A schematic design of the evaporator	34
2.17	A ncAFM image of NaCl on KBr with the histogram of the height distribution of NaCl on KBr	35
3.1	Growth modes of thin films	37
3.2	Isotherms of the different growth modes and the different kinetic pro- cesses that can happen at the surface	39

3.3	Reflectivity of the steps with their resulting growth mode	41
3.4	Non-contact AFM topography of NaCl on Cu(100) showing the growth mode	43
3.5	Non-contact AFM topography of NaCl on Cu(100)	44
3.6	Non-contact AFM of the end of film of NaCl	45
3.7	Kink and edge atoms	47
3.8	Steps orientation and Smoluchowski effect	49
3.9	NaCl stripes on Cu(100)	53
3.10	Growth of NaCl on Cu(211)	55
3.11	Non-contact image NaCl/Cu(111)	56
4.1	Contact AFM, overviews of the NaCl film	58
4.2	Contact AFM, NaCl islands	60
4.3	Bias voltage for NaCl and Cu	61
4.4	Contact AFM, overviews of the NaCl film and copper	62
4.5	Friction contrast over a NaCl island	63
4.6	Lateral force versus normal force (schematic diagram)	64
4.7	Tomlinson simulation of atomic-scale stick-slip	65
4.8	Stick-slip over a NaCl island	66
4.9	Friction coefficient of alkali halides versus their film thickness	68
4.10	Stick-slip measurements on NaCl(100)	70
A.1	A technical drawing of the UHV system	73
B.1	Auger spectrum of copper	74
C.1	Schematic design of the holder for the crucible.	75
C.2	Schematic design of the shutter.	76
C.3	Top view of the shutter plate.	76

List of Tables

2.1	The pressure range of the different degrees of vacuum	6
2.2	Auger intensity for different NaCl coverage	17
2.3	Parameters for the fitted gaussians of the histogram in figure 2.17(b)	35

Chapter 1

Introduction

In the following sections, an history of tribology throughout the different periods of mankind's history is presented. Dowson has presented an extensive review of the history of tribology and the following is inspired by his book, *History of Tribology* [1].

1.1 History and origin of tribology

According to the *Oxford English Dictionary* [2], tribology is "the branch of science and technology concerned with interacting surfaces in relative motion and with associated matters (as friction, wear, lubrication, and the design of bearings)" and the word tribology has been suggested by C. G. Hardie of Magdalen College in 1965. Thus, even though tribology as been studied for a long time, the term itself is fairly recent. Historically, the advent of tribology comes from as far back as the Stone Age [10^6 to 10^3 years ago]. Throughout history, tribology has played an extremely important role in the advent of the various technologies that we rely on in today's society.

The Stone Age has seen the birth of the *homo sapiens* and with the development of tools, the birth of tribology. Using the percussion of flint stones or the friction of wood on wood, humans had gained control over the fire and were discovering frictional heating. The development of tools brought the elaboration of the first plain bearings.

The appearance of the early civilizations [3500 B.C. to A.D. 1500], the Sumerians, the Egyptians, the Mesopotamians, civilizations from the Indus Valley, and the Chinese, has led to the development of new tools such as drills and wheels. Lubricants started appearing in applications involving translation and rotation, such as the use of water lubricated sleds for the transportation of stone building blocks. The gear appeared around 600 B.C. in China. The Romans and the Greeks [900 B.C. to A.D. 400] brought philosophy and the organization of science. The first mechanical systems were built including lathes, wheeled transport, pulleys, cranes and mills of various kind. The first scientific books were written which included the subject of tribology. Also, the first ball-bearings were designed and used to improve the performances of battering rams. The Middle Ages [400 to 1450] (sometimes referred to as the Dark Ages) saw the increased use of metal instead of wood in the fabrication of bearings and the emergence of more complex mechanical systems such as clocks.

During the Renaissance [1450 to 1600], the advent of printing brought the possibility to develop organized communication between the science community of the different emerging "nations". A man named Leonardo da Vinci did the first recorded scientific studies on friction, wear, gears, bearings and lubricants. He introduced the concept of the coefficient of friction as being the ratio of the friction force to the normal load and envisioned bearings which are astonishingly similar to their modern analogue. Just before the Industrial Revolution [1600 to 1750], progress in the realization of the importance of friction and wear for the development of machinery was made. Although little advancement was reported on lubricants, a more fundamental knowledge was gained on the friction processes: Newton's laws of classical mechanics and its hypothesis on viscous flow, and the concept of asperities interactions was introduced by Amontons (1699).

The Industrial Revolution [1750 to 1850] brought the steam machine (James Watt, 1769) and the development of a new mean of transportation: the train. A tremendous expansion of the field of tribology along with a lot of branching was necessary

to face the challenges of this new era. The use of greases and lubricants in metal bearings increased their lifetime and their effectiveness. These times have seen more fundamental studies on friction and the beginning of fundamental studies on wear and lubrication, with Coulomb receiving *Le Prix de l'Académie des Sciences* in 1781 for his work on friction. The Post Industrial Revolution [1850-1925] brought the discovery of mineral oils with a burst in the studies on lubrication. The theory of fluid-film lubrication brought awareness that lubricating films of thickness in the range of 10^{-9} to 10^{-5} m were needed for the successful operation of sliding machine elements. It is during this period that inventions which make use of tribology appeared such as the automobile and the steam-turbine-driven ship.

Recently [1925 to present], the tremendous industrial development has led to an increased demand for a better understanding in all areas of tribology. Even though the general trend points in the direction of wear and friction reduction, some examples of productive wear and friction are parts of our everyday life such as writing with a pencil, breaks on cars and other means of transportation and bolts and nuts. In the last thirty years, the advent of computers and the miniaturization of electronics components have demanded an increasing urge for the comprehension of tribology on a smaller scale leading to the development of nanotribology. [3]

1.2 Friction at the nanoscale

At the macroscopic scale, friction is known to be independent of the geometric contact area and proportional to the load. On the other hand, friction on the nanoscale differs greatly from what has been observed at the macroscale. The friction force microscope (FFM) brings the possibility to study the friction of contacts consisting of single or very few asperities. In the nanoscale regime, the friction depends on the contact area and is velocity dependent. The gap between the friction at macroscopic scale and at the nanoscale can be bridged by using the fact that at the macroscale, the contact between two materials is not made between the total surface of the two bodies in

contact but rather by a sum of microscopic asperity contacts. When considering these asperity contacts, the friction at the macroscale becomes dependent of the contact area. [3, 4]

1.3 Nanotribology

Recent developments in nanotechnology have led to the development of a "new" field: nanotribology (also referred to as microtribology, molecular tribology or atomic-scale tribology). At such small scales, the conditions are really different than with conventional macrotribology. The loads, which are usually big in macrotribology, are very small in nanotribology. Wear is reduced to a few atomic layers and in nanotribology surface properties dominate while in macrotribology the bulk properties of the material are more relevant. The tools that led to the birth of this field are mainly the scanning tunneling microscope (STM), developed by Binnig et al. in 1981, the atomic force microscope (AFM), also developed by Binnig et al. in 1986, and the friction force microscope (FFM), also called the lateral force microscope (LFM), which was developed by Mate et al. in 1987 and is a modification of the AFM. All these and other instruments based on STMs and AFMs are referred as scanning probe microscopes (SPMs). Some of these along with the relevant instrumentation for the resented project will be presented in the following chapter. [3, 4]

Chapter 2

Instrumentation

2.1 Surface science methods

Surface science is a field of science that developed quite recently, basically starting in the early 1960s, with the combination of the developments in vacuum technology, surface analysis techniques and the advent of computers. Relevant to the presented project are many surface science tools such as ultrahigh vacuum system, surface preparation techniques, low energy electron diffraction, Auger electron spectroscopy, and force microscopy and scanning probes. All of these will be discussed throughout this chapter. [5]

2.1.1 Ultrahigh vacuum

The study of clean surfaces at the atomic level is impossible under atmospheric conditions. This is because chemical reactions at the surface occur at a very high rate at this pressure. These reactions alter the composition of the surface thus contaminating the sample to be studied. In order to be able to preserve the sample from contamination, one should reduce the interactions between the surface and its environment. It should also be noted that some of the techniques used to probe the surface use charged particles which interact strongly with gas-phase molecules. In order for these charged particles to reach their target and be detected properly one has to minimize

Degree of vacuum	Pressure range (mbar)
low	$10^3 > P < 3.3 \times 10^1$
medium	$3.3 \times 10^1 \geq P < 10^{-3}$
high	$10^{-3} \geq P < 10^{-6}$
very high	$10^{-6} \geq P < 10^{-9}$
ultrahigh	$10^{-9} \geq P < 10^{-12}$
extreme ultrahigh	$10^{-12} \geq P$

Table 2.1: The pressure range of the different degrees of vacuum (table from [7]).

the interference from gaseous molecules. [6]

There are different ways of reducing the rate of interactions (reducing the temperature of the environment would be one) and reducing the number of gas molecules in the vicinity of the sample is a very effective method. This can be achieved by studying the sample in a vacuum chamber which has the desired analytical equipment attached to it. A description of the vacuum chamber used for the experiment presented in this thesis can be found in section 2.2.

To obtain an estimate of the pressure necessary to reach for a surface science experiment on a clean surface one can start with the approximation that the quantity of molecules adsorbed at the surface should not exceed a few percent of a monolayer in about an hour (a typical time to perform an experiment). The pressure calculated from this approximation is of the order of 10^{-10} mbar [5, 6, 8, 9, 10]. Although this is assuming the worst case scenario (i.e. a surface with a sticking coefficient of unity), many interesting surfaces (like metals) fall into that range. It is appropriate to classify the different degrees of vacuum: low, medium, high, very high, ultrahigh, and extreme ultrahigh. The range of pressure for these degrees of vacuum can be found in table 2.1. Note that often low and medium are merged as low, high and very high as high, and ultrahigh and extreme ultrahigh as ultrahigh.

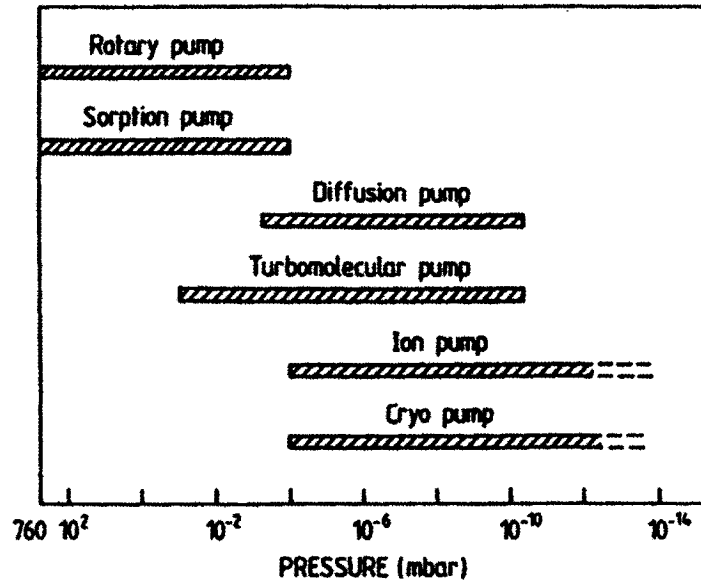


Figure 2.1: Operating pressure range for different types of pumps (from [8]).

To achieve such ultrahigh vacuum conditions, a system of high performing pumps is necessary. Different types of pump have different ranges of operation so they need to be separated by valves as a pump that has reached its operating pressure acts as a leak for other pumps. The most widely employed pumps in today's UHV systems are rotary pump, sorption pump, diffusion pump, turbomolecular pump, ion pump and cryo pump. Their respective range of operating pressure can be seen in figure 2.1. From this figure one can see that in order to obtain pressure below 10^{-10} mbar a combination of at least two pumps is required. Description of how they work is widely available in literature and the reader should refer to it if necessary. [5, 8]

Pressure gauges are required to ensure proper monitoring of the pressure in the chamber. There exist different types of gauges operating over different pressure ranges. Two main categories of manometer exist: direct gauges and indirect gauges. Direct gauges measure the force of the flux of particles impinging on a wall (wall displacement) while indirect gauges measure a pressure dependent property of the gas. In direct gauges, the wall is either solid, such as a diaphragm gauge, capacitance manometer, Bourdon tube, and Radiometer, or liquid, such as a U-tube manometer,

and McLeod gauges. The list of indirect gauges is much more extensive. There are three categories of indirect gauges: momentum transfer (viscosity), charge transfer (ionization), and energy transfer (thermal conductivity). The most common momentum transfer gauge is the spinning rotor and it is suitable for medium vacuum pressure measurements ($< 10^{-5}$ mbar). The most common energy transfer gauges are the thermocouple and the Pirani gauges and they are suitable for medium vacuum pressure measurement ($> 10^{-3}$ mbar). The charge transfer gauges consist mainly of hot cathode (Bayard-Alpert, extractor) which are suitable for high vacuum pressure measurements, and cold cathode (Penning) which are suitable for ultrahigh vacuum pressure measurements. It is important to note that one can monitor the composition of the remaining gas in the chamber using a residual gas analyzer which can act at the same time as a leak detector. Most of the high and ultrahigh vacuum gauges are not suitable for higher pressure so a combination of two or more gauges is required to monitor the pressure in the chamber at all time. [5, 7, 8]

It is also important to note that UHV conditions cannot be reached without bake-out of the chamber. Every part of the chamber that comes in contact with air whenever the chamber is vented is covered by a thin water (H_2O) film. These water molecules are very sticky to many surfaces because of their high dipole moment. With time they will slowly desorb from the surface and will prevent the pressure to drop lower than $\sim 10^{-8}$ mbar. [8] Also, molecules imprisoned in the bulk of the wall of the chamber diffuse in to the chamber, adding to the system's pressure. As diffusion is exponentially related to the temperature, heating the chamber accelerates the diffusion process hence reducing the diffusion at ambient temperature. The bake-out process consists of heating the chamber and the equipment to $125^\circ C$ for about 24 hours. This ensures that most of the water molecules desorb from the walls and get pumped out of the chamber. [5, 8]

2.1.2 Sample preparation

As surface science experiments are highly sensitive to contaminants, techniques to clean samples inside the vacuum chamber are required. Bombarding the surface with ions of a noble gas (the most common being Ar^+) removes the substrate top layers along with contaminants. Albeit a very effective technique, argon atoms often get adsorbed by the surface and also destroy the crystalline structure of the surface. Annealing is thus necessary to remove the embedded atoms and restore the surface structure. [5, 6, 8]

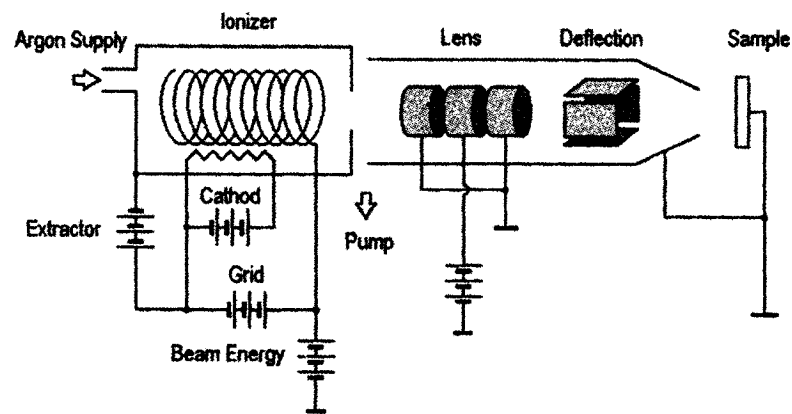


Figure 2.2: Schematic diagram of a noble gas ions sputter gun (from [8]).

The procedure for one cycle of sputtering/annealing is as follow (refer to figure 2.2 for a schematic diagram of a noble gas ions sputter gun). First the gas is admitted to the ion gun through a leak valve. Electrons emitted from the cathode collide with the noble gas producing ions. The ions are then accelerated by the desired voltage and directed towards the surface of the sample. A set of lenses is used to focus the beam of ions. The annealing part of the cycle consists of heating the sample to about 2/3 of its melting temperature. For copper, the annealing temperature is around 900°K . Heating to such a temperature is done by electron bombardment from behind the sample (note that resistive heating can also be used). A heated filament provides the electrons and the sample is biased to a voltage of about 2000 V. The first time a sample is cleaned in vacuum, several cycles of sputtering/annealing are required as

impurities from the bulk can diffuse to the surface during the process but once the surface has been cleaned using this technique later cleaning procedures require less cycles.

Another very useful technique to prepare a clean sample is cleavage. This technique consist of removing the exposed part of the crystal to exhibit a fresh, unexposed part of the bulk crystal. Crystals can be cleaved simply by aligning a long sharp object (e.g. a razor blade) along a crystalline plane direction and applying an instantaneous pressure (e.g. hitting the razor blade with a hammer). The crystal will break along the desired direction and the surface will then be clean and ready for surface science experiments. This technique can be used to prepare, for example, a clean surface of KBr.

2.1.3 Low energy electron diffraction

A common diffraction technique for surface characterization is low energy electron diffraction (LEED). As its name claims, structural information is acquired from the analysis of low energy electrons, scattered elastically from the surface of the sample. The energy range used for LEED (typically 30 to 200 eV) is so that the electron wavelengths are of the order of or less than the interatomic distances. Also the mean free path of these electrons is short, hence elastic collisions occur only in the very top layers of the studied sample. The obtained diffraction pattern is directly related to the crystal reciprocal lattice:

$$\mathbf{k} - \mathbf{k}_0 = \mathbf{G}_{\mathbf{hkl}} \quad (2.1)$$

where \mathbf{k} is the scattered wave vector, \mathbf{k}_0 is the incidence wave vector and $\mathbf{G}_{\mathbf{hkl}}$ is a reciprocal lattice vector.

Figure 2.3(a) shows a schematic diagram of a standard four-grid LEED set-up. The electrons are emitted from a cathode filament, which is at a potential $-V$. This is followed by a Wehnelt cylinder and a set of electrostatic lenses to focus the beam of electrons. The cathode filament along with the Wehnelt cylinder and the electrostatic

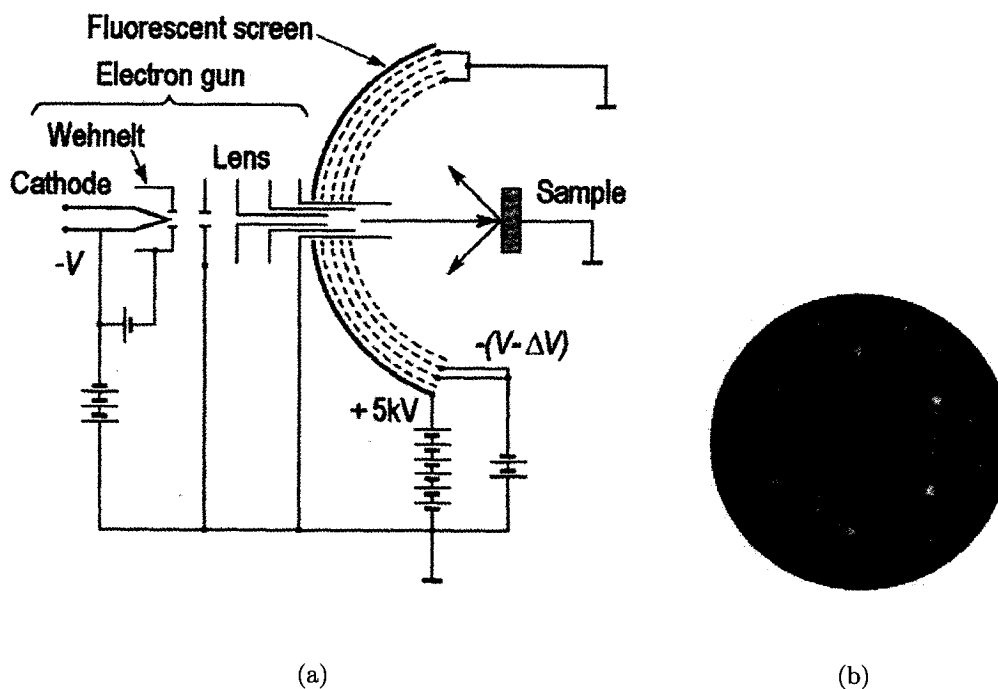


Figure 2.3: a) A schematic design of a standard four-grid LEED set-up (from [5]) b) A typical LEED pattern exposing a Si(111) 7×7 surface (from [5]).

lens are referred to as the electron gun. The last aperture of the lens, the sample, and the first grid are at earth potential, accelerating the electrons to the desired energy before the scattering of the electrons from the sample. The purpose of the second and third grid (retarding grids) is to filter out the inelastically scattered electrons and are at a potential of $-(V - \Delta V)$. Adjustment of ΔV , the retarding voltage, is used to get the highest spot-to-background contrast. After passing the retarding grids, the electrons are reaccelerated by the fluorescent grid, on which the diffraction pattern can be observed, which is typically biased at a voltage of +5 keV. The fourth grid's, which is at earth potential, purpose is to screen the other grids from the potential of the fluorescent screen.

A LEED pattern can be interpreted using its different features, namely the spot sharpness, the spot geometry, the spot profile and recording the so called $I-V$ curves. The LEED pattern consists of bright, sharp spots and low background intensities.

Structural defects and crystallographic imperfections on the surface of the sample lead to broadening and weakening of the spots and increases the background intensity. Hence the sharpness of the spots can be used to characterize the perfectness of the crystalline surface. One can use spot geometry to determine the lattice structure of the sample. Bright spots, called the integer-order, represent the lattice structure (cubic, rhombohedral, etc) while the lighter spots, called superspots or extra-spots, represent a superstructure formed at the surface. On figure 2.3(b), one can see that the bright spots exhibits the hexagonal structure of the silicon while the lighter spots represent the reconstructed 7×7 structure. One can use the spot profiles, by analyzing the intensity distribution across the width of a spot, to gain more information about surface imperfections as the spot profile is disrupted by any deviation from the ideal 2D periodicity. Finally, the position of atoms can be evaluated by analysis of the spot intensity as a function of the primary electron energy, called the $I-V$ curves.

2.1.4 Auger electron spectroscopy

Auger electron spectroscopy (AES) is an electron spectroscopy technique which, by using the energy spectra of the secondary electrons emitted from the sample when bombarding it with electrons with typical energies in the range of 5 to 5000 eV, characterizes the electronic structure of the surface of the sample. This particular range of energies is used because the electrons with such energies are strongly scattered in solids, hence the sensitivity of this technique. AES can be used to verify the cleanliness of a surface prepared in UHV. It is also used for study of film growth, surface chemical (elemental) analysis, and depth profiling of the concentration of particular elements (for that particular application, alternating cycles of sputtering and AES are required). It is important to note that AES is a surface sensitive technique because of the limited escape depth of electrons. Thus, the typical probing depth of AES is of the order of 1 nm to 3 nm. Bombarding a sample with electrons of defined energy (E_P , the primary energy) creates a secondary electron spectrum. This spectrum exhibits a sharp elastic peak at the primary energy, a broad peak near $E = 0$ showing no particular structure and a long region where there is few electrons

between E_P and $E = 0$ which shows a number of tiny peaks. These tiny peaks are the important peaks for electron spectroscopy and can be separated in two categories: loss peaks which are primary electrons that have lost a discrete amount of energy (studied using electron energy loss spectroscopy), and peaks of fixed energies which are independent of the primary energy. The latter are the peaks studied using AES. The spectra are recorded by an electron energy analyzer, as either $N(E)$ (number of emitted electrons), $dN(E)/dE$ or $d^2N(E)/dE^2$ versus energy (E). [5, 8]

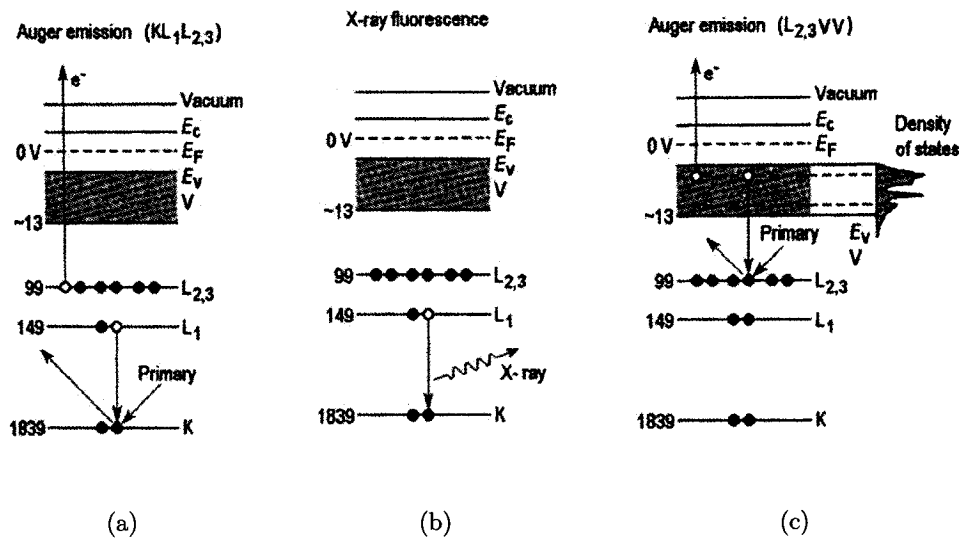


Figure 2.4: a) Auger emission ($KL_1L_{2,3}$), the incident electron strikes an electron in the K-shell which is then replaced by an electron from the L_1 -shell and an electron from the $L_{2,3}$ -shell is ejected b) X-ray fluorescence, the incident electron creates a hole in the K-shell and an electron from the L_1 -shell replaces it and releases an X-ray photon c) Auger emission ($L_{2,3}VV$), the incident electron hits an electron in the $L_{2,3}$ -shell which is then replaced by an electron from the valence band and an electron from the valence band is ejected (from [5]).

When the incident electron strikes an atom on the surface, it creates a core hole and both electrons leave the atom, leaving the atom ionized. The created hole is then filled by an electron from a higher level but the ionized atom is still in a highly excited state.

It will relax back to a lower energy state either by the emission of a characteristic X-ray photon (X-ray fluorescence), or by a radiationless Auger transition in which the electron that changes level transfers its gained energy to another electron of the same shell or of a different shell. The latter is then emitted with a characteristic Auger energy. Thus the atom is left in a double-ionized state with two holes in the same (or different) core level. Figure 2.4(a) and 2.4(c) both shows Auger emission processes while figure 2.4(b) shows a X-ray fluorescence process. The same level notation is used in both X-ray and Auger (K, L₁, L_{2,3} and V for the valence band). The Auger transition is characterized using the location of the initial hole and the location of the final two holes. One can use the binding energies of the level involved in the transition to determine the kinetic energy of the ejected atom. For example, the kinetic energy of the ejected electron in figure 2.4(a) can be estimated as

$$E_{KL_1L_{2,3}} = E_K - E_{L_1} - E_{L_{2,3}} - \phi \quad (2.2)$$

where $\phi = E_{\text{vacuum}} - E_{\text{Fermi}}$ is the work function of the material. [5, 8]

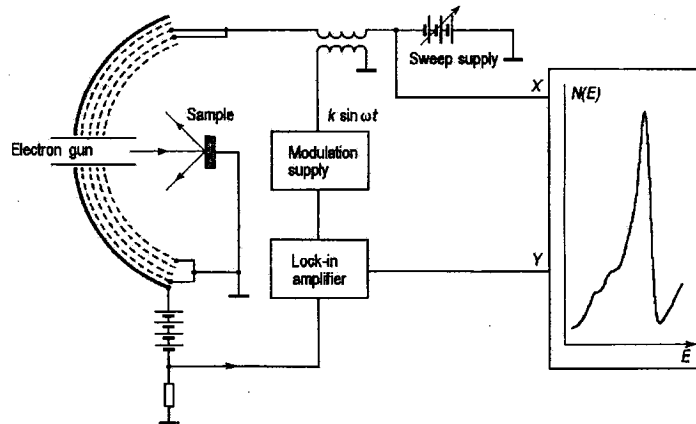


Figure 2.5: Schematic representation of an Auger set-up. In this particular set-up, AES is combined with LEED, hence the four-grid energy analyzer (from [5]).

The standard equipment for AES consists mainly of an electron gun, an energy analyzer and the data processing electronics. Figure 2.5 shows a schematic diagram of

a typical four-grid retarding field analyzer (LEED and AES combined). The primary electron beam is produced by the electron gun with energy between 1 to 5 keV. The energy analyzer is the four-grid analyzer as in LEED. Using detection at the frequency ω results in recording the spectra in the $N(E)$ mode, while recording of the spectra in the $dN(E)/dE$ spectra can be achieved by detecting at 2ω . Typically, recording of the $dN(E)/dE$ signal is preferred because it suppresses the large background of true secondary electrons and thus improves peak visibility. The differentiation of the signal is performed by superimposing a small alternating voltage $\Delta U = k \sin(\omega t)$ to the two inner grids and modulating the analyzing energy with this voltage. Hence

$$I(E_0 + k \sin \omega t) \simeq I_0 + \frac{dI}{dE} k \sin \omega t - \frac{d^2 I}{dE^2} \frac{k^2}{4} \cos 2\omega t \quad (2.3)$$

gives the recorded current. [5, 8]

Auger electron spectroscopy offers the possibility of doing quantitative analysis. This means that the measured Auger intensities can be used to determine the number of atoms of a certain species present on the surface. The current obtained from an atom species i is given by

$$I_i = I_P \sigma_i \gamma_i (1 + r_i) T \frac{1}{4\pi} \iiint n_i(z) \exp\left(\frac{-z}{\lambda_i \cos \theta}\right) \sin \theta \, d\theta \, d\phi \, dz \quad (2.4)$$

where I_P is the intensity of the beam of primary electrons, $\gamma_i(jkl)$ is the probability of relaxation by the jkl Auger transition, $(1 + r_i)$ is the backscattering factor which include the backscattering of primary electrons and secondary electrons, $n_i(z)$ is the number of atoms i as a function of the depth z , and the exponential term accounts for the probability of no-loss escape of Auger electrons from depth z . In this exponential term, $\lambda_i(E_{jkl})$ is the electron attenuation length and the angle θ is the escape angle of the Auger electron with respect to the normal of the surface. T represents the transmission of the energy analyzer. [5]

Now to get the Auger intensities of a system where there is a layer of thickness d_A of a material A on a substrate B , equation 2.4 has to be modified. First, to mathematically describe the system, the concept of atomic fraction of the different

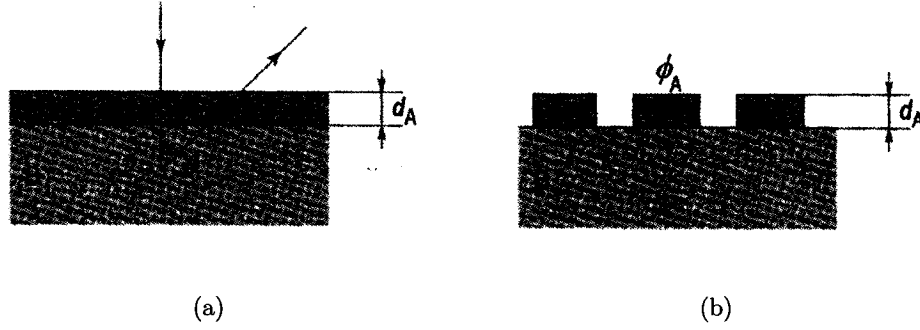


Figure 2.6: A deposited film A on a substrate B . a) The surface of the substrate is fully covered with the thin film and b) the surface of the substrate is partially covered with the thin film (from [5]).

materials needs to be introduced. X_A represents the fraction of A in the system while X_B represents the fraction of B . It is then obvious that $X_A + X_B = 1$ over the whole system. For a film of material A covering the substrate B , one gets

$$X_A(z) = \begin{cases} \phi_A & \text{if } 0 < z \leq d_A \\ 0 & \text{if } z > d_A \end{cases} \quad X_B(z) = \begin{cases} 0 & \text{if } 0 < z < d_A \\ 1 & \text{if } z \geq d_A \end{cases} \quad (2.5)$$

where in the case of the film covering the whole substrate as in figure 2.6(a) $\phi_A = 1$ and in the case of only partial coverage of the substrate by the film (by a fraction α), $\phi_A = \alpha$ as shown in figure 2.6(b). Then, integrating equation 2.4 over z using the preceding condition, one gets that the intensities of the Auger peaks for the different materials are given by

$$I_A = I_A^\infty \frac{1 + r_B(E_A)}{1 + r_A(E_A)} \phi_A \left(1 - \exp \left[\frac{-d_A}{\lambda_A(E_A) \cos \theta} \right] \right) \quad (2.6)$$

$$I_B = I_B^\infty \left(1 - \phi_A \exp \left[\frac{-d_A}{\lambda_A(E_B) \cos \theta} \right] \right) \quad (2.7)$$

where I_A^∞ and I_B^∞ are the elemental sensitivity factors for the elements A and B and can be found in handbooks or by performing calibration experiments. [5]

The intensity of the Chlorine peak for different coverage of deposited NaCl can be made by considering the backscattering factors of NaCl and Cu to be similar and the

ϕ_{NaCl}	I_{Cl}	I_{Cu}
0.025	0.003	0.244
0.05	0.007	0.238
0.075	0.010	0.233
0.1	0.014	0.227
0.15	0.021	0.215
0.2	0.027	0.204
0.3	0.041	0.181
0.4	0.055	0.158
0.5	0.069	0.135
0.6	0.082	0.112
0.7	0.096	0.089
0.8	0.110	0.066
0.9	0.123	0.043
1.0	0.137	0.020

Table 2.2: The calculated intensity of the Cl (equation 2.8) and Cu (equation 2.9) Auger peak for different NaCl coverage of the Cu surface.

angle of reflection (θ) to be 0° . Hence equation 2.6 reduces to

$$I_{\text{Cl}} = I_{\text{Cl}}^\infty \phi_{\text{NaCl}} \left(1 - \exp \left[\frac{-d_{\text{NaCl}}}{\lambda_{\text{NaCl}}(E_{\text{Cl}})} \right] \right) \quad (2.8)$$

$$I_{\text{Cu}} = I_{\text{Cu}}^\infty \left(1 - \phi_{\text{NaCl}} \exp \left[\frac{-d_{\text{NaCl}}}{\lambda_{\text{NaCl}}(E_{\text{Cu}})} \right] \right) \quad (2.9)$$

the different value being $I_{\text{Cl}}^\infty = 1$ [11], $I_{\text{Cu}}^\infty = 0.25$ [11], $d_{\text{NaCl}} = 0.28$ nm (the thickness of one monolayer of NaCl) [12], $\lambda_{\text{NaCl}}(E_{\text{Cl}}) = 19$ Å [13], $\lambda_{\text{NaCl}}(E_{\text{Cu}}) = 34$ Å [13], $E_{\text{Cl}} = 181$ eV [11], and $E_{\text{Cu}} = 920$ eV [11]. Table 2.2 shows the intensity of the peak of Chlorine for different coverages of NaCl on the copper substrate. Thus one can see that the Chlorine peak is expected to be visible for coverage as low as a quarter of a monolayer.

2.1.5 Scanning probe microscopy and other imaging techniques

Aside from SPM methods there are other surface science techniques to image the surface structure. Some of them have a resolution down to the nanometer scale and even sometimes can acquire images with atomic resolution. The information that can be obtained with these techniques concerns the surface crystallography, the surface morphology, and the surface composition. The most common of these microscopy techniques are the field emission microscope (FEM), the field ion microscope (FIM), the transmission electron microscope (TEM), the reflection electron microscope (REM), the low-energy electron microscope (LEEM), and the scanning electron microscope (SEM). [5]

The scanning probe microscopy (SPM) field comprises microscopy techniques which use a tip to scan a surface and produce a real-space image of that surface. Scanning probes use a near-field interaction between the surface and the probe as a basic physical principle. The development in 1981 of the scanning tunneling microscope (STM) by G. Binnig and H. Rohrer was the starting point of the SPM family. The STM was so successful that they received the Nobel prize for physics in 1986 for

the development of this new tool. The most commonly used techniques of the SPM family are the STM, the atomic force microscope (AFM) and its modified version, the friction force microscope, and the magnetic force microscope (MFM). These tools bring the possibility of performing local experiments with single atoms or molecules and can be used for a wide range of applications including force measurements of single chemical bonds and measurements of the friction at the atomic scale, to name a few. [4, 5]

Scanning tunneling microscope

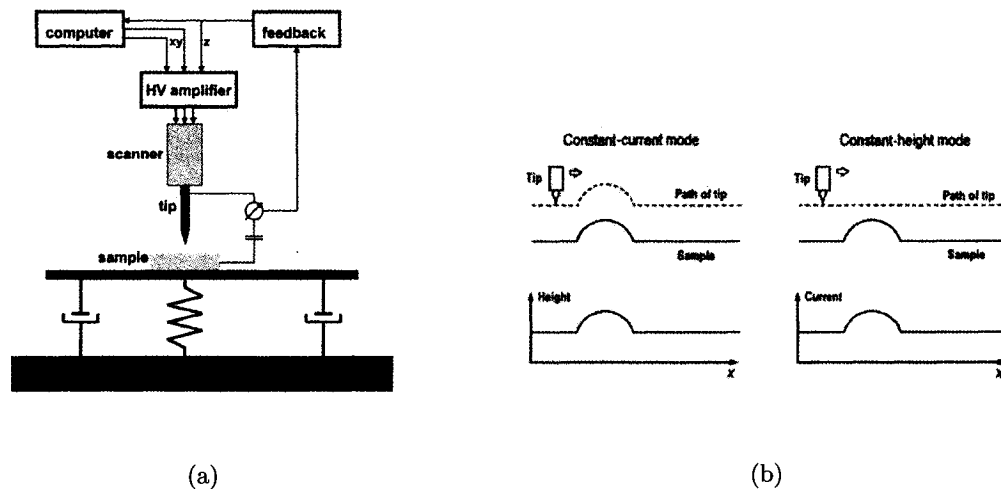


Figure 2.7: **a)** Schematic representation of STM (from [4]), **b)** The two main modes of STM operation. In the *constant current mode*, I_T and V are kept constant while z is recorded as a function of x and y and in the *constant height mode*, z and V are kept constant while I_T is recorded as a function of x and y (from [5])

The STM is based on the tunneling of electrons between a sharp metallic tip and the surface. The tunneling current (I_T) can flow from the tip to the sample or from the sample to the tip depending on the sign of the applied bias voltage (V). Since the tunneling current is a quantum mechanical effect, the tip and the surface must be separated by a really small distance, typically of the order of 5 to 10 Å. Tunneling current is a powerful near-field interaction but it has one major flaw: it can only occur

between two conducting surfaces. Hence, the studied surface must be conducting. A basic setup of a STM is shown in figure 2.7(a). The tip is scanned across the surface in x and y and the data is recorded by the computer. The height of the probe (with respect to the sample surface) is changed using piezoelectric actuators which are controlled by the feedback electronics via a high-voltage amplifier. Depending on the mode of operation used, the tip is controlled by either the tunneling current (constant current mode) or by the height of the probe (constant height mode) as represented in figure 2.7(b). The constant current mode is particularly useful for scanning surfaces which are not necessarily atomically flat but it has a limited scan speed due to the slow response of the system that adjusts the vertical position of the tip. The constant height mode can scan the surface faster and can thus be used for studying real-time dynamic processes. Since the vertical position of the tip is not adjusted with the different features of the surface, this mode can only be used on relatively flat surfaces. [3, 4, 5, 8]

Force microscopy

A few years after the development of the STM, Binnig, Quate and Gerber developed the AFM, in 1986. The basic principle behind the AFM is rather simple. An extremely sharp tip, located at the end of a comparatively long cantilever, is scanned across the sample surface. The interatomic forces between the sharp tip and the surface atoms cause the cantilever to be deflected and this deflection is monitored, hence allowing the surface topography to be imaged. The deflection of the cantilever can be monitored using different techniques, the most common being the reflection of a light beam on the rear-side of the cantilever and its detection by a position-sensitive photodiode (4-quadrant photodiode). Other techniques include using the cantilever as part of an optical laser interferometer, detecting a change in the capacitance between the cantilever and a counterelectrode, and self-sensing cantilevers such as cantilever with built-in piezoresistance circuitry. In the original AFM design by Binnig *et al.*, the deflection of the cantilever was monitored by a STM tip located above the cantilever. Figure 2.8(a) shows the basic setup of an AFM. AFM has the advantage

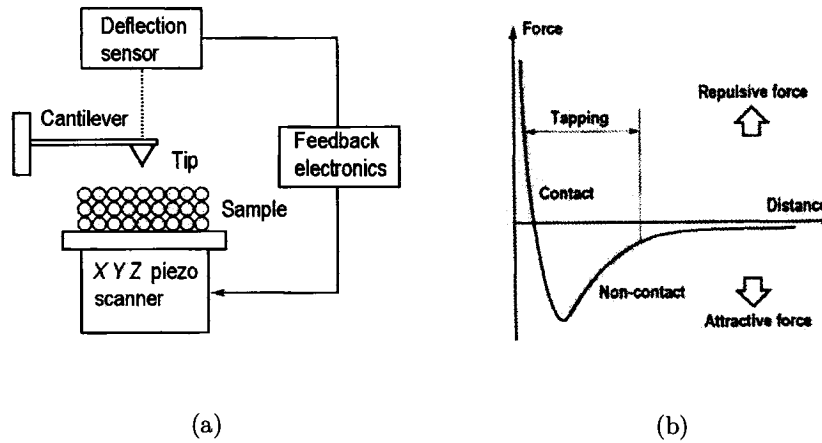


Figure 2.8: a) A schematic representation of a basic AFM setup. The cantilever is scanned across the surface and its deflection is recorded by a deflection sensor. The deflection signal is then used to control the tip (or the sample) with the piezo scanner. b) The different modes of operation of the AFM with respect to the van der Waals force on the interatomic distance. The contact mode is based on repulsive forces, the non-contact mode senses attractive forces and repulsive forces (in particular electrostatic forces and magnetic forces) [14], and the tapping mode exploits both repulsive and attractive forces (from [5]).

over the STM that it can be used to study all type of surfaces, being conducting, semiconducting, or insulating. [3, 4, 5]

Different forces act between the sample / cantilever-tip system. Short-range forces (forces that arise from repulsion of the ions core and from the overlap of the electron wave functions), van der Waals forces, electrostatic forces, magnetic forces and capillary forces are among them. Note that in most case magnetic forces can be neglected. For an AFM operating in UHV conditions capillary forces can be neglected too. Short-range forces become comparable to long-range forces at a distance of about 0.5 nm, a characteristic distance for the achievement of atomic resolution in non-contact mode. They can be both repulsive and attractive. Van der Waals and electrostatic forces are long-range forces and always have to be taken into account

in force microscopy. Van der Waals forces are dipole-dipole forces that for single molecules decay inversely proportional to the distance to the 7th. One can get an estimate of the van der Waals forces in force microscopy by approximating the tip as a sphere approaching a semi-infinite body. In that case

$$F_{\text{vdW}} = \frac{HR}{6D^2} \quad (2.10)$$

where H is the Hamaker constant (10^{-19} J), R is the radius of the sphere (tip), and D is the distance between the sphere and the semi-infinite body (tip-sample distance). For a tip of a radius of 30 nm at a distance of 0.5 nm from the sample, the van der Waals forces are about 2 nN. The electrostatic forces act between localized charges on insulating tip and samples. Charges can be trapped at the surface during the preparation of the surface with techniques such as cleaving and ions sputtering. For a tip approximated as a truncated cone and a half sphere the electrostatic forces are given by

$$F_{\text{el}} = \pi\epsilon_0 \frac{R}{z} (U_{\text{bias}} - U_{\text{cpd}})^2 \quad (2.11)$$

where R is the radius of the half-sphere, z is the tip-sample distance, U_{bias} is the bias voltage applied between the tip and the sample, and U_{cpd} is the contact potential difference caused by the work function at the tip and sample. For a tip radius of 20 nm, a sample distance of 0.5 nm, and $U_{\text{bias}} - U_{\text{cpd}} = 1$ V, the electrostatic forces are about 0.5 nN. [4]

Meyer, Hug and Bennewitz provided an extensive description of the different modes of an AFM [4]. Basically, one can sort out the modes in two categories, static and dynamic mode, and by specifying if the tip is in contact with the surface or not. The static mode consists mainly of the contact mode and the static deflection mode (constant height mode). The dynamic mode measures change in the vibrational properties of the cantilever due to tip-sample interactions, such as eigenfrequency, oscillation amplitude and the phase between excitation and oscillation of the cantilever. Note that the feedback parameters used for distance control permits to differentiate the different dynamic modes. The so-called non-contact AFM or dynamic force microscopy

(DFM) uses the frequency shift of a self-exciting cantilever as a feedback parameter. Another dynamic mode is the tapping mode. This is when one excites a cantilever with an amplitude of several nanometers close to its resonance frequency. For this project, the contact mode and the non-contact AFM mode have been used and hence will be presented with greater details in the next paragraphs.

The contact mode is a static mode, in which the topographic images are recorded by scanning the tip over the surface at constant cantilever deflection. There are many forces acting in contact mode. There is the attractive force between the mesoscopic cantilever and the sample, the repulsive force between the tip apex and the sample, and the external force exerted by the cantilever spring. For the tip to be in at constant cantilever deflection, these forces have to constantly be in equilibrium. The deflection corresponds to a normal force which is obtained by multiplying the spring constant of the cantilever with the deflection signal. In contact mode, topography images usually are images of constant repulsive force. One has to note that the local variations in the elasticity of the surface can influence the measurements. Usually, after the tip is brought in contact, one can minimize the forces by retracting the cantilever, i.e. applying a negative load. When scanning the surface in contact mode, the tip-sample contact also produces a lateral force on the tip apex which causes a torsional bending of the cantilever. One can thus study the local variation of friction with a high resolution. The variation of the local friction should produce an inverted contrast in forward and backward scans. [4]

Non-contact AFM (also called dynamic force microscopy) can produce images which are comparable to STM quality. It is also possible to achieve true atomic resolution with this mode of operation. In this mode the cantilever is mechanically excited at its eigenfrequency. Tip-sample interactions produce frequency shifts and this frequency shift is what is used to control the tip-sample distance. The oscillation amplitude is either control by a constant excitation amplitude, and hence the oscillation amplitude is damped as the cantilever approaches the surface, or it is controlled by maintaining

a constant amplitude in all experimental situations, which makes stable operation of the instrument harder to achieve, but permits the quantitative analysis of the forces [4]. In the experiment presented in this project, the oscillation amplitude was controlled by maintaining a constant amplitude. [4]

2.2 Ultrahigh vacuum system

The ultrahigh vacuum (UHV) system used to create the UHV environment in this project is a commercial UHV system purchased from Omicron Vakuumphysik GmbH [15]. This system consists of an analysis chamber and a sample introduction chamber. Attached to the chamber is a four-grid LEED/AES, an ion sputter gun, an electron beam sample heater, a resistive sample heater and a three-axis manipulator. The chamber with the Scanning force/tunneling microscope described in the following section is attached to the analysis chamber. The sample introduction chamber can be isolated from the other parts of the system by means of a valve to permit sample introduction without contaminating the whole vacuum system. The system is brought to UHV pressures by a set of four pumps, namely a roughing pump, a turbopump, an ion getter pump, and a Titanium sublimation pump. A technical drawing of the vacuum system is presented in appendix A.

2.3 Scanning force/tunneling microscope

The scanning force microscope (SFM) used during this project has been homebuilt at the University of Basel in Switzerland. The design on which it is based is described in an paper by Howald *et al.* [16] It is designed for operation in ultrahigh vacuum. It is a combined SFM/STM which hence permits to perform measurements on a wide variety of samples. The normal and lateral forces acting on the cantilever tip are measured by optical deflection of the light from a light emitting diode (LED) which is fed in the vacuum chamber through an optical fiber. The reflected light from the cantilever is directed to a four-quadrant photodiode by means of two mirrors which

are mounted on spherical steel balls. The balls can be moved by feeding a sawtooth voltage signal to three piezo plates which are in contact with the balls. The probing tip is mounted on a tip holder to facilitate vacuum manipulations. The studied sample is mounted on a sample plate for the same reason and this sample plate is mounted on the end of a tube scanner that can move the sample in three dimensions [16]. This set-up is then mounted on a slider which is moved by three piezo plates for coarse positioning of the sample. The vibrational damping is achieved by suspending the whole stage on which the instrument lies with four springs. Additional damping based on eddy currents is provided by adding a ring of radial copper lamellae floating between a ring of permanent magnets. [16].

2.4 Copper sample

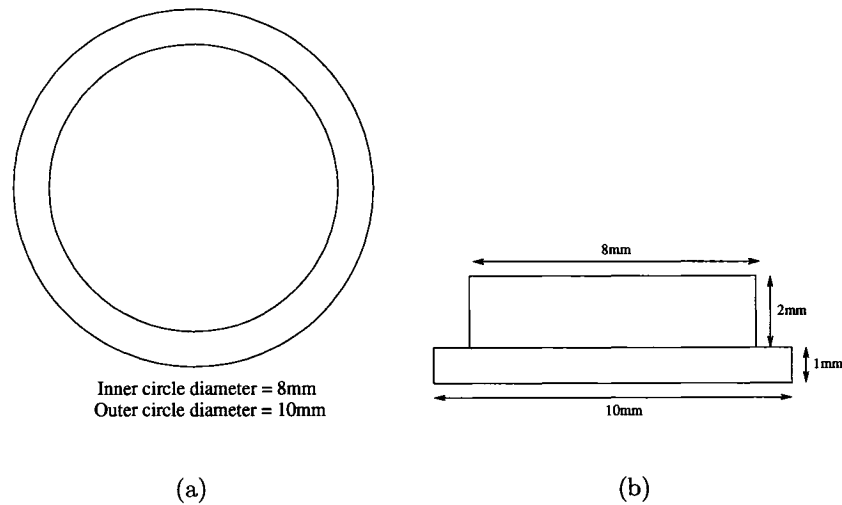


Figure 2.9: a) Top view and b) side view of a schematic representation of the copper sample.

To achieve the goal of evaporating salt on a copper substrate, a copper sample was ordered from MaTecK GmbH [17]. The sample is a single crystal, showing the Cu(100) surface, of very high purity (99.999%). It is designed such that it has a hat shape (see figure 2.9): a 8 mm disk on top of a 10 mm disk. The top disk is 2 mm

thick while the bottom part is 1 mm thick. The top part has been polished to have an overall roughness of less than $0.03 \mu\text{m}$ and an orientation accuracy (miscut) of less than 0.1° with respect to the (100) plane. This ensures that the surface of the sample will consist of monoatomic terraces of a relatively large size. The average terrace's size (l_{terrace}) can easily be estimated using a right-angle triangle and the fact that the copper interlayer spacing is 0.18037 nm [18]:

$$l_{\text{terrace}} = \frac{0.18037 \text{ nm}}{\tan(0.1)} = 103.34 \text{ nm} \quad (2.12)$$

Hence one can expect to have terraces that are of the order of 100 nm in size.

2.4.1 Sample holder

As mentioned before, this experiment is performed in UHV. This means that a sample holder compatible with the chamber must be used to hold the copper sample. A sample holder for silicon oxide samples was available but had to be modified to fit the purchased copper sample. First of all, the silicon sample holder was disassembled and the unneeded pieces were stored for future use. The only useful piece is in fact the sample holder plate which has four M1.2¹ screw holes already drilled in it. Figure 2.10(b) shows the bare silicon sample holder plate with a projection of the copper sample on top of it. A quick calculation using right-angle triangle ensures that the sample will effectively fit between the screws:

$$d = \sqrt{(8.34 \text{ mm})^2 + (10.25 \text{ mm})^2} = 13.21 \text{ mm} \quad (2.13)$$

so there is a tolerance of about 3 mm. To fit the sample on the plate, a Molybdenum sheet of a thickness of 0.5 mm was machined 2.10(c) according to the dimensions taken from the silicon sample holder and the copper sample diameter. Molybdenum threaded rods, nuts and washers were used to fix the sample with the sheet on the sample plate. The resulting copper sample holder is pictured in figure 2.10(d). In the design of the copper sample holder, molybdenum parts were used because of the low

¹this is an indication of what screw type to use for this hole, in this particular situation, a 1.2 mm screw

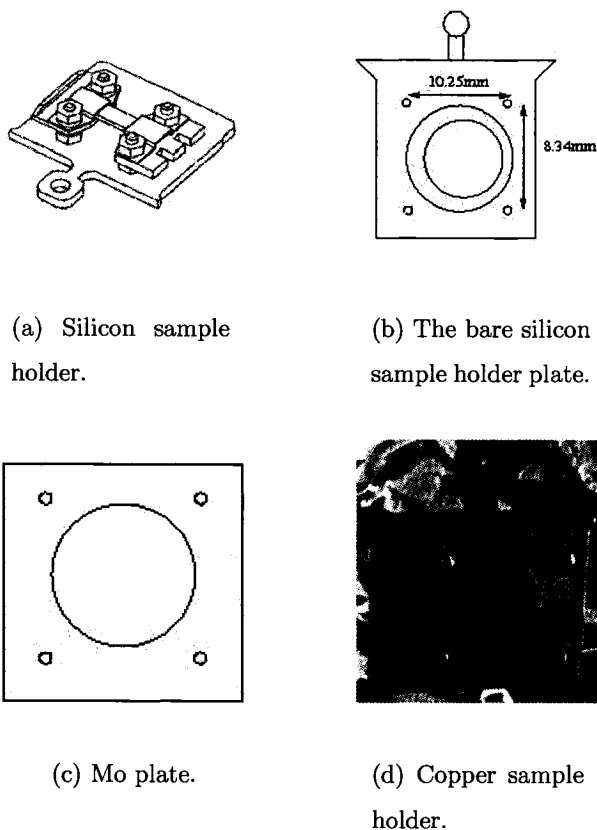


Figure 2.10: a) The silicon sample holder, b) the bare silicon sample holder plate which was used to make the copper sample holder, c) the Molybdenum plate used to hold the copper sample on the copper sample holder and d) the copper sample holder with the mounted copper sample.

outgassing rate of this metal, the high purity of the molybdenum material available commercially and also because of the high melting point of this material (2890°K [17]). It is in fact very important to use parts that can sustain high temperature as the copper sample (hence the sample holder) need to be heated to about 725°K as part of the cleaning process of the sample (see section 2.4.2). With this, the copper sample can now be safely inserted in the chamber and different experiments can be performed to characterize this surface.

2.4.2 Preparation of the copper surface

The copper surface was prepared by repeated cycles of low-energy argon-ion bombardment and annealing in UHV. The argon-ion bombardment was done at 1000 eV and the annealing at a temperature of 450°C. Usually only two cycles were necessary to prepare a clean (100) copper surface. Different methods to verify how clean the surface can be prepared have been used and are explained in section 2.4.3. This is in accordance with the method to prepare a clean Cu(100) surface in UHV described in [6] on page 76. [8, 19, 20]

2.4.3 Characterization of the copper surface

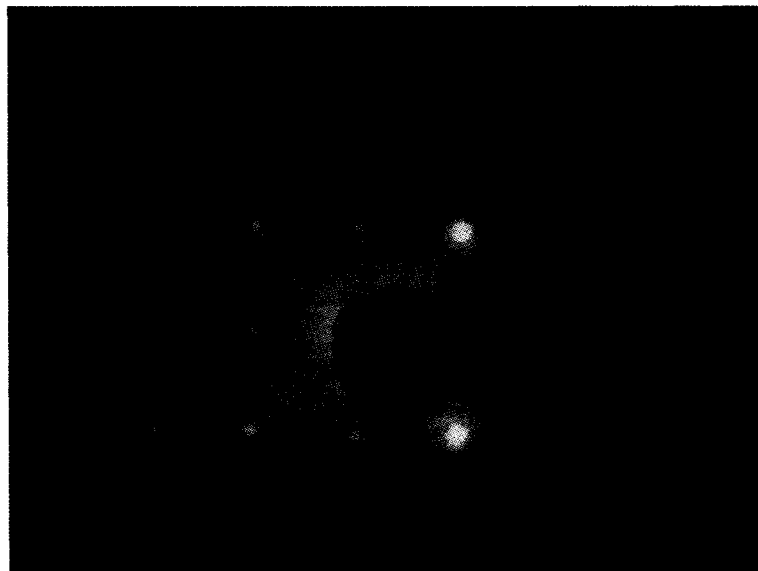


Figure 2.11: A typical LEED image of the copper surface exposing the (100)-direction of the surface. One can note that the (100)-direction of the surface is parallel to the x-axis (which is parallel to the horizontal direction of the page). The electron energy used when recording this image was 105 eV.

The copper surface was characterized using LEED, AES and STM. The crystal structure can be verified using LEED, the purity using AES and the average terrace size can be checked using STM.

A typical LEED image is shown in figure 2.11. The conclusion that can be drawn from this image is that the surface is effectively a (100) surface and that it makes an angle of approximately 0° with respect to the AFM/STM, i.e. the atoms are parallel with the horizontal border of the image taken with this instrument.

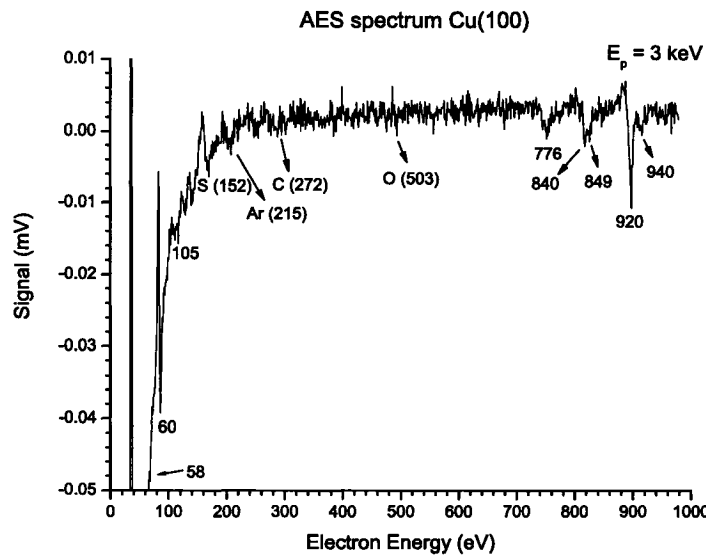


Figure 2.12: A typical AES spectrum of the copper sample.

The figure 2.12 exhibits a typical AES spectrum. The numbers refer to the characteristic peaks for copper unless specified. The peaks of the typical contaminants of copper can be recognized. Comparing it with the spectrum from the Handbook of Auger Electron Spectroscopy [11] (see figure B.1 in appendix B), one can conclude that the characterized sample contains a very low amount of impurities. Hence, the purity of the sample can be established to be very high.

The STM images (figure 2.13(a) and 2.13(b)) show the bare copper sample. Looking at the two images one can see that the average terrace size is lower than the size of 100 nm calculated in equation 2.12. It can be evaluated to be around 60 nm. From that one can determine the miscut to be $\sim 0.17^\circ$ which is close to twice the the

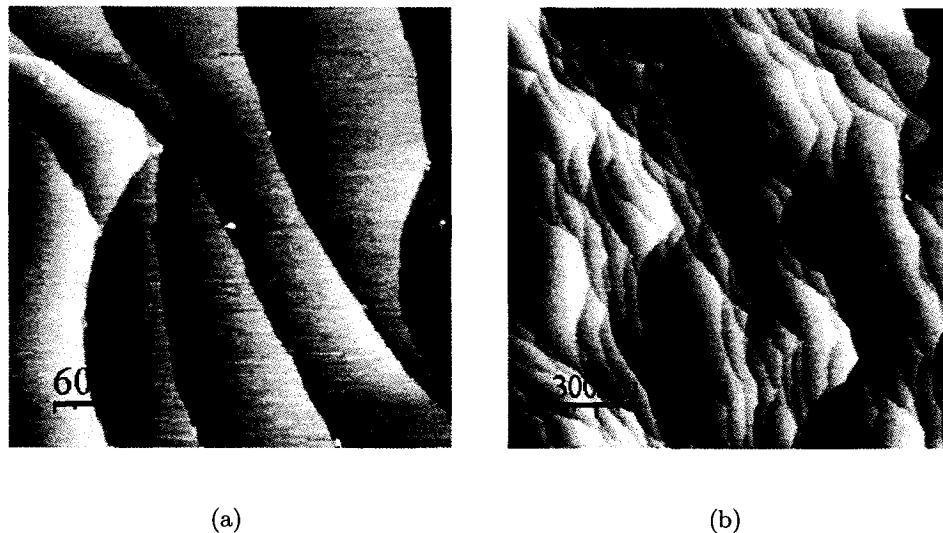


Figure 2.13: Typical STM image of the copper sample of size a) 300 nm and b) 1500 nm.

miscut specified in the data sheet of the sample. These are typical images from the bare copper sample and are rather easy to obtain by simply approaching the tip anywhere around the sample. Some comments on the sensitivity of the AES can be made by counting the number of pinning steps on a determined area. In figure 2.13(a), 6 pinning steps can be counted in a $90\,000\text{ nm}^2$ area. There are approximately 16 copper atoms per nm^2 , hence there are approximately 1.44×10^6 atoms in total shown in this frame. Thus the ratio of impurities per atoms in this area is $6 / 1.44 \times 10^6$ and is surely too small to measure with AES.

2.5 Homebuilt evaporator

To achieve the goal of taking friction measurements on ultra-thin films of salt, a method to evaporate the NaCl in the vacuum chamber must be thought of. Commercially, there are some products available called Knudsen cells (or evaporator). Evaluating the cost of commercially available evaporators, it soon became obvious that a homebuilt evaporator would be cheaper. In that respect, a list of characteristics must first be determined in order to settle on what to buy and what to build.

This will be the first part of this section. Furthermore, a description of the design will be presented, followed by the fabrication itself. Finally, the testing of this home-built evaporator will be presented.

2.5.1 Characteristics

To properly build an evaporator, the desired characteristics have first to be determined. First of all, this evaporator will be part of an UHV system and hence must be UHV compatible. Thus all the parts must have a very low outgassing rate and must be able to sustain very low pressure. Also, in order to evaporate salt, it has to be heated up to at least 375°C, so the parts must be able to tolerate temperature of that order. Temperature control is a must, consequently a temperature measurement system has to be incorporated in the instrument. In order to limit the effect of evaporated particles on the overall pressure in the UHV chamber and to limit the contamination of the sample by evaporating impurities that might be present in the salt, a closed compartment to heat the salt must be designed. This compartment would stay closed during the heating process and opened only when the desired temperature is reached. These are the basic characteristics that are needed to build an evaporator that will be able to achieve the desired goal of evaporating NaCl on a copper substrate.

2.5.2 Design and fabrication

To start with, the evaporator must be attached to the chamber such that the salt has a clear path to the sample. Thus an empty flange must be chosen keeping in mind that the evaporator can't be pointed down (or else the salt will be spilled in the chamber when the heating compartment is opened) and it must point at the front of the sample holder to reach the polished face of the copper sample. With these requirements in mind, a 70 mm flange was chosen (see figure A.1 in appendix A). Hence the evaporator must be built to fit a rather small flange and space limitations will be a major concern when constructing/buying parts.

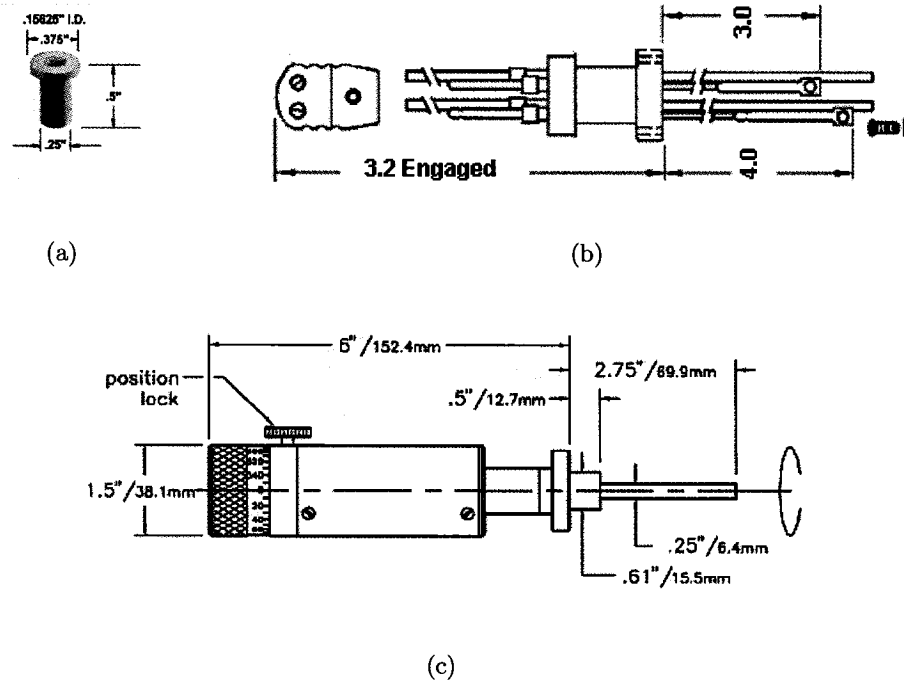


Figure 2.14: Three different parts used to build the evaporator. a) The crucible, b) the power/thermocouple feedthrough and c) the rotary motion (from [21]).

The compartment for the salt which was chosen is a cylindrical quartz crucible of 0.375" inner diameter (figure 2.14(a).) In order to be able to evaporate the salt and also to measure the temperature during the heating process, a power/thermocouple feedthrough (see figure 2.14(b)) was selected. The salt is heated by wrapping a filament around the crucible and by passing a current through the filament by means of the power/thermocouple feedthrough. The filament is a tungsten wire of a diameter of 0.5 mm which can easily be formed around the crucible. The temperature is measured by connecting thermocouple wires (type K, e.g. chromel and alumel wires) and by placing it in the crucible. The temperature is monitored by means of a Labview program which was programmed by Sabine Maier. The power needed to heat the filament is provided by a power supply which came with the Omicron UHV system. The crucible can be closed and opened by adding a shutter (see figure C.2 in appendix C) made from a molybdenum sheet (thickness of 0.5 mm) above the crucible opening. This shutter is connected to the rotary motion hence making

it possible to rotate it from the outside of the vacuum chamber. This ensures that the salt will only be evaporated when it has reached the proper temperature thus keeping the contamination of the sample low. Figure 2.14(c) shows the rotary motion feedthrough. Note that the crucible, the power/thermocouple feedthrough and the rotary motion were ordered from Kurt J. Lesker Company [21].

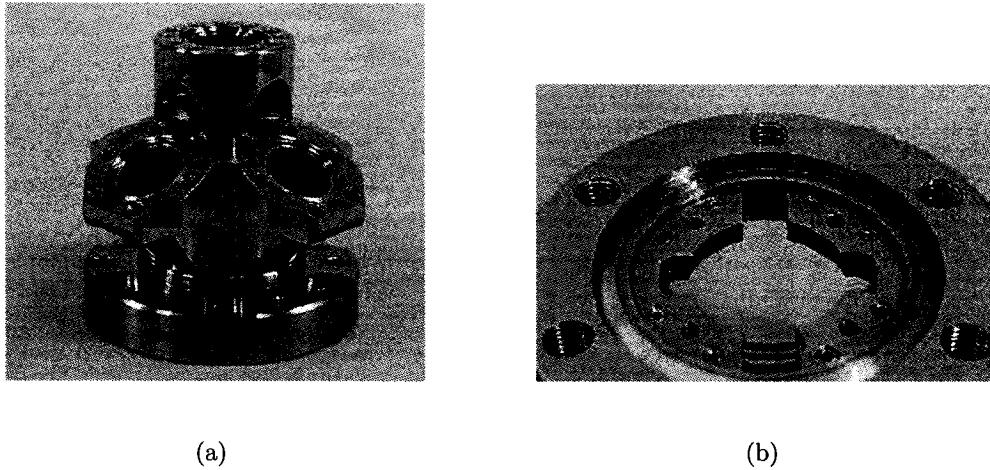


Figure 2.15: a) The multiple flange adapter and b) the groove grabbers.

Now these feedthroughs are fitted to a 70 mm flange. A multiple flange adapter (see figure 2.15(a)) was found to be commercially available at Kimball Physics Inc. [22]. This will make it possible to properly fit two 35 mm flanges (the power/thermocouple and the rotary motion feedthroughs) on one 70 mm flange. The next step is to mount the crucible on this flange adapter. Luckily, the flange adapter has grooves in its inner part which allow groove grabbers (see figure 2.15(b)) to be attached to it which, in their turn, have built in threaded holes. These threaded holes will make it possible to build a socket for the crucible (see figure C.1 in appendix C) and attach it to the flange of the evaporator.

A schematic design of the evaporator is presented in figure 2.16. Note that the shutter is a few millimeters away from the crucible to leave space for the thermocouple wires which are going inside the crucible and to allow for effective pumping of the

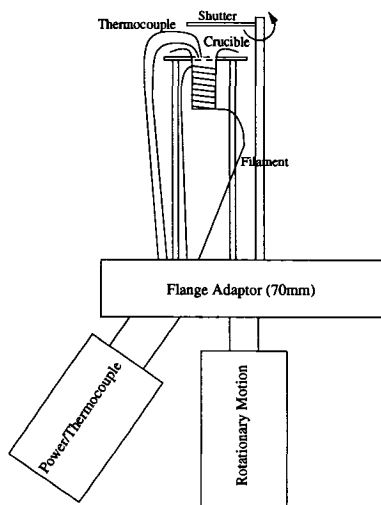


Figure 2.16: A schematic design of the evaporator.

crucible. The shutter has been attached to the rotationary motion by means of a long threaded rod and a set screw (see figure C.2 in appendix C). The last part of the building of the evaporator is to attach it to the vacuum chamber. Thus, the blank 70 mm flange is removed and replaced by the evaporator. As mentioned before, the space is restricted and the evaporator is a tight fit in the chamber. Hence, once in place, one has to use a multimeter to ensure that neither the thermocouple nor the filament is shorting with the chamber walls.

2.5.3 Testing and calibration of the evaporator

Once in place on the vacuum chamber, the evaporator needs to be tested to properly determine its characteristics. By making a simple model of the vacuum chamber, an approximate sample position can be determined. The position can then be optimized by trials and errors, using AES to compare the salt coverage of the copper sample. The fact that the salt can be detected by AES confirms that the evaporator is working properly. Note that during the first evaporation pressure rose from $\sim 1 \times 10^{-10}$ mbar to $\sim 1 \times 10^{-8}$ mbar. This was expected as the NaCl in the crucible contained humidity from being exposed to ambient air. During the subsequent evaporations the pressure rose from $\sim 1 \times 10^{-10}$ mbar to $\sim 5 \times 10^{-10}$ mbar in part due to the increased

Parameters	KBr	NaCl
y_0 (fixed)	0	0
height	0.14008 ± 0.00052	0.41734 ± 0.00056
width (ω)	0.08698 ± 0.00133	0.09397 ± 0.00155
Intensity (number of counts)	45.83429 ± 0.54144	25.97455 ± 0.32657

Table 2.3: Parameters for the fitted gaussians of the histogram in figure 2.17(b).

temperature in the chamber and because of the NaCl particles being evaporated.

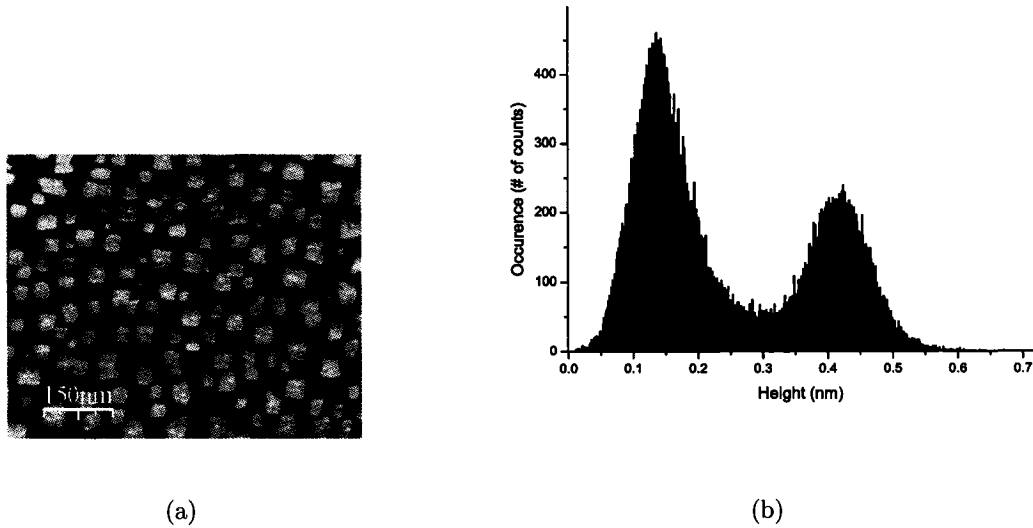


Figure 2.17: a) A ncAFM image of NaCl on KBr with b) a histogram of the height distribution of NaCl on KBr.

For the calibration of the evaporator, one needs to determine the total coverage of salt on the sample with respect to the time of evaporation. Since the evaporation is conducted at a fixed temperature, only the time of evaporation affects the coverage of the sample. Concerning the homogeneity of the NaCl flux from the evaporator, one should note that at the scale at which the surface is studied ($\sim 1\mu\text{m}$), the flux is certainly homogeneous. Note that if one would need to evaporate at another temperature, the calibration would need to be performed again, but throughout the

different experiments detailed in this document, the evaporation was conducted at a temperature of 500°C. A KBr(100) single crystal surface was used to calibrate the evaporator as NaCl grows in a Volmer-Weber mode (islands) on this surface with islands of monoatomic height (see figure 2.17). Then a height distribution analysis was performed on a typical image to determine the height of each points on this image. The fitted gaussians (see figure 2.17(b)) of the histogram obtained reveal the intensity of the respective peaks corresponding to KBr and NaCl. By comparing these intensities, available in table 2.3, one get that the corresponding coverage of NaCl on KBr is:

$$\frac{I_{\text{NaCl}}}{I_{\text{NaCl}} + I_{\text{KBr}}} = \frac{25.97}{71.80} = 36.17\% \quad (2.14)$$

Thus, about 1/3 of a monolayer of NaCl is grown on the surface in a time of 20 minutes at a temperature of 500°C. The following calculation has been performed on another image from a different evaporation, leading to a similar result of coverage ($\pm 2\%$). Taking into consideration that the closing / opening is a human process, the error on the opening / closing time is of the order 5 seconds. Also, over the course of the evaporation the temperature of the filament fluctuates about 5 degrees Celsius under and above 500°. Thus one can estimate the error on the coverage to be around 5% making the coverage $36.0\% \pm 2.5\%$, or about a third of a monolayer.

Chapter 3

Experiments

3.1 Growth modes

3.1.1 Interfacial energies

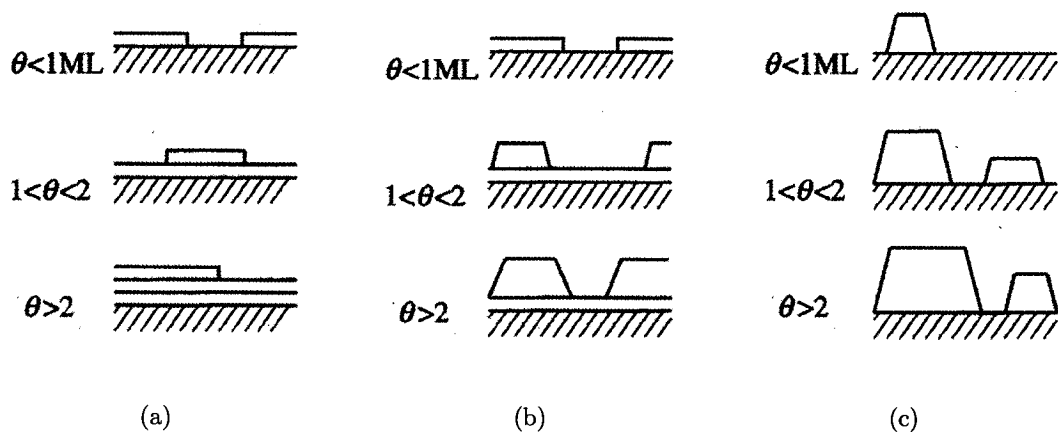


Figure 3.1: Schematic representation of the different growth modes (from [23]): a) Frank-van der Merwe, b) Stranski-Krastanov (islands start to grow after one layer), c) Volmer-Weber.

The deposition of a substance A on a substrate B can lead to three different growth modes (figure 3.1): Frank-van der Merwe or layers, Stranski-Krastanov or layers-plus-islands and Volmer-Weber or islands. The different modes arise because

the substance A is either more attracted to itself than to the substrate B , which leads to Volmer-Weber growth, or it is more attracted to the substrate than it is to itself, which leads to Frank-van der Merwe growth. Stranski-Krastanov growth is an intermediate growth mode where the addition of layers increases the interface energy (γ^*). After a finite amount of layers have been deposited on the surface, the deposited atoms become more attracted to each other than to the surface, thus leading to a transition from layers growth to islands growth. In terms of surface energy the different growth modes can be expressed as follow: Frank-van der Merwe growth arises whenever

$$\gamma_A < \gamma_B + \gamma^* \quad (3.1)$$

where γ_A is the surface energy of the substance A and γ_B is the surface energy of the substrate B , Volmer-Weber growth arises when

$$\gamma_A > \gamma_B + \gamma^* \quad (3.2)$$

and finally Stranski-Krastanov growth can be expressed as follow

$$\gamma_A < \gamma_B + \gamma^* \xrightarrow{\text{layers-to-islands}} \gamma_A > \gamma_B + \gamma^* \quad (3.3)$$

In the latter, it is important to point out that the islands grow on top of the layers and that in some cases less than a monolayer of deposited material will result in layers-plus-islands with some regions of the surface exposing the substrate and some regions exposing the deposited material. Also note that in layers growth, the layer is strained to more or less fit the substrate. When it fits perfectly it is called pseudomorphic growth. [24, 25]

An adsorption isotherm can be associated with each growth mode: figure 3.2(a) for Frank-van der Merwe, figure 3.2(b) for Stranski-Krastanov and figure 3.2(c) for Volmer-Weber. Also, several kinetic processes occur on the surface during film growth. Upon arrival, the adatom can then diffuse on the surface, nucleate with a peer, re-evaporate, bind at special sites (such as steps, impurities, etc.) and interdiffuse (see figure 3.2(d)). Note that this description of the different growth modes with respect

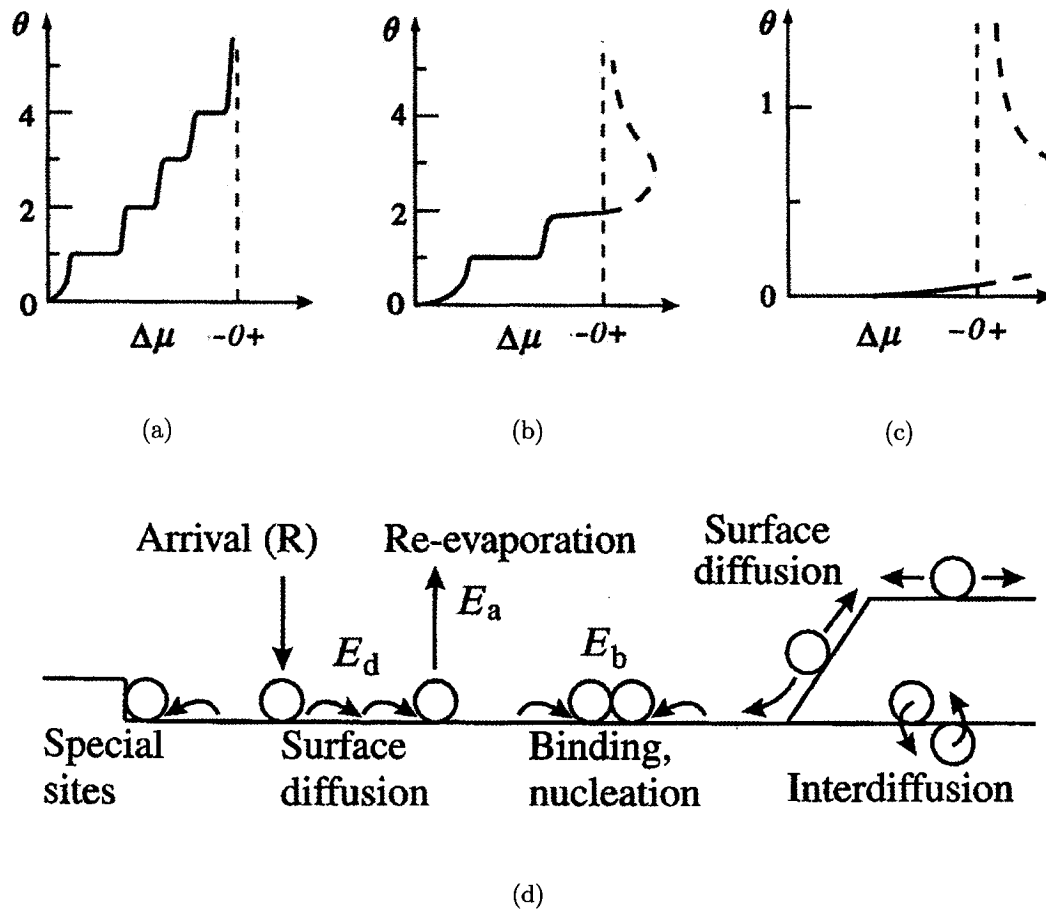


Figure 3.2: Adsorption isotherms for the different growth modes a) Frank-van der Merwe, b) Stranski-Krastanov (islands start to grow after two layers), c) Volmer-Weber and d) the different kinetics processes that can happen at the surface (from [23]).

to the interfacial energies assumes that the system is in equilibrium. When the system is not in equilibrium, one has to consider the reflectivity of the steps or their trapping properties in order to give an accurate description of why the different growth modes occur.

3.1.2 Reflectivity of lattice steps

Another picture for explanation of the three growth modes presented in figure 3.1 is to introduce the concept of the reflectivity of lattice steps. First of all, one has to realize that lattice steps play an important role in the diffusion of adatoms on the surface. When using the minimization of the interface energies to explain the different growth modes, one has to realize that this explanation uses the equilibrium thermodynamic properties, while often the studied epitaxial layers have not reached an equilibrium. Annealing of the surface is often required to reach such equilibrium. Hence, one has to consider the behavior of diffusing adatoms on the surface. As underlined in the previous section and in figure 3.2(d), adatoms can undergo different processes upon arrival on the substrate surface, the most important being diffusion on the different surfaces, either the substrate surface or the deposited film surface. This will be addressed in the following paragraph.

When an adatom encounters a step edge, it can come from two sides of the step: the descending step, called an α -step (α -side of the step), and the ascending step, called a β -step (β -side of the step). It shall be noted that α - and β -steps have identical reflectivity to epitaxial growth [25], thus in the following the α -step will only be considered. α -steps can either reflect a diffusing adatom, and thus it will remain on the same terrace, or if the step is non-reflective, the diffusing adatom will go across the step and be incorporated into the step edge. To start diffusing on the "new" terrace, the adatom need to overcome a potential barrier and thus it will most likely stay incorporated into the step edge. Overall, there are three possibilities (as there are numbers of growth modes) for the reflectivity of the steps. If the α -steps are always reflective then the film will grow in 3D islands (Volmer-Weber mode). If the α -steps are non-reflective then the film will grow in 2D layers (Frank-van der Merwe mode). The last possibility needs the concept of heterosteps and homosteps to be introduced: heterosteps are two neighboring steps made of different material and homosteps are two neighboring steps made of the same material. If in the substrate-film system the heterosteps are non-reflective but the homosteps are reflective then

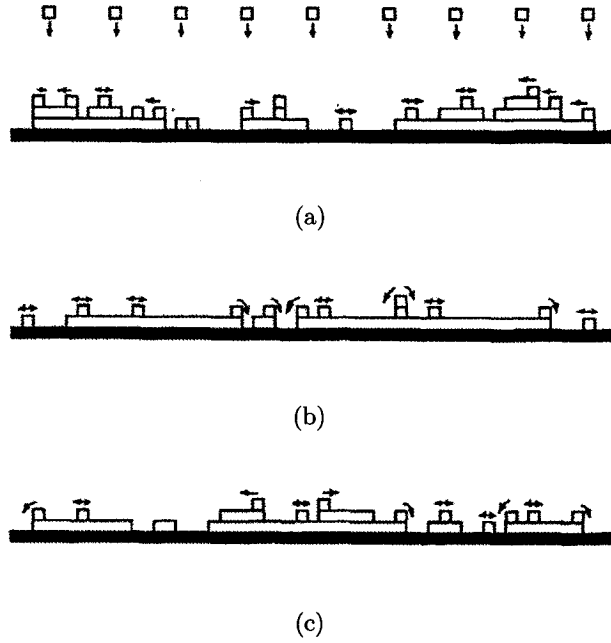


Figure 3.3: Schematic representation of the reflectivity of the steps with their resulting growth mode: **a)** α -steps are always reflective thus the growth mode is Volmer-Weber **b)** α -steps are non-reflective thus the growth mode is Frank-van der Merwe and **c)** heterosteps are non-reflective but homosteps are thus the growth mode is Stranski-Krastanov (from [25]).

the growth mode will be of the mixed type (Stranski-Krastanov mode). Figure 3.3 shows a schematic representation of the reflectivity of the steps and their resulting growth modes. Note that the reflectivity of the α - and β -steps are only important in low substrate temperature epitaxy, i.e. temperatures where the binding energy of step edge atoms is high enough that the dissociating rate of step edge atoms is low. In higher substrate temperature, the trapping strength of the step edge is the determining factor of the growth mode. In the presented project, the experiment has been performed at room temperature, hence the reflectivity of the steps should play an important role in the determination of the growth mode. [25, 26]

3.2 Growth mode of ultrathin films of NaCl on Cu(100)

To study the growth mode of NaCl on Cu(100), an ultrathin film of NaCl has to be deposited on a Cu(100) substrate. The growing of a crystalline film of one material on the crystalline substrate of another material referred to as heteroepitaxy, in contrast with homoepitaxy where the deposited material is the same as the substrate material [5]. The growth mode of ultrathin films of NaCl on the Cu(100) substrate has been mainly studied using an AFM in non-contact mode. The deposition of NaCl on the substrate has been achieved by molecular beam epitaxy (MBE). MBE relates to the evaporation of a material from an effusion cell or an evaporator. The rate of evaporation was estimated to be about 1 monolayer per hour as described in section 2.5.3 on page 34. An evaporation of 1/3 of a monolayer (20 minutes) has been performed on the copper sample. Thus, the studied surface will exhibit parts covered with the NaCl film and parts where the copper substrate is still visible. Hence the prepared surface will make it possible to determine the growth mode of NaCl on Cu(100).

3.2.1 Non-contact AFM topography of NaCl on Cu(100)

Figure 3.4 exhibits typical non-contact AFM images taken after the evaporation described above. The relevant features in these images are the following. The first monolayer of NaCl grows over the copper substrate in a large island, of typical size of $500 \times 500 \text{ nm}^2$ or more. This large island lies over the copper substrate steps like a carpet. The copper steps are still clearly visible under this layer. On top of the first monolayer, the NaCl grows in regular square shape islands, well-oriented on the substrate. Based on the description and the representation (figure 3.1) of the different growth modes, one can conclude that NaCl grows in a Stranski-Krastanov mode on the Cu(100) substrate. The typical size of the NaCl islands is about 20 nm to 50 nm. One can also see that the NaCl islands have a preference for growing over the underlying copper steps. Another observation is that where the first monolayer

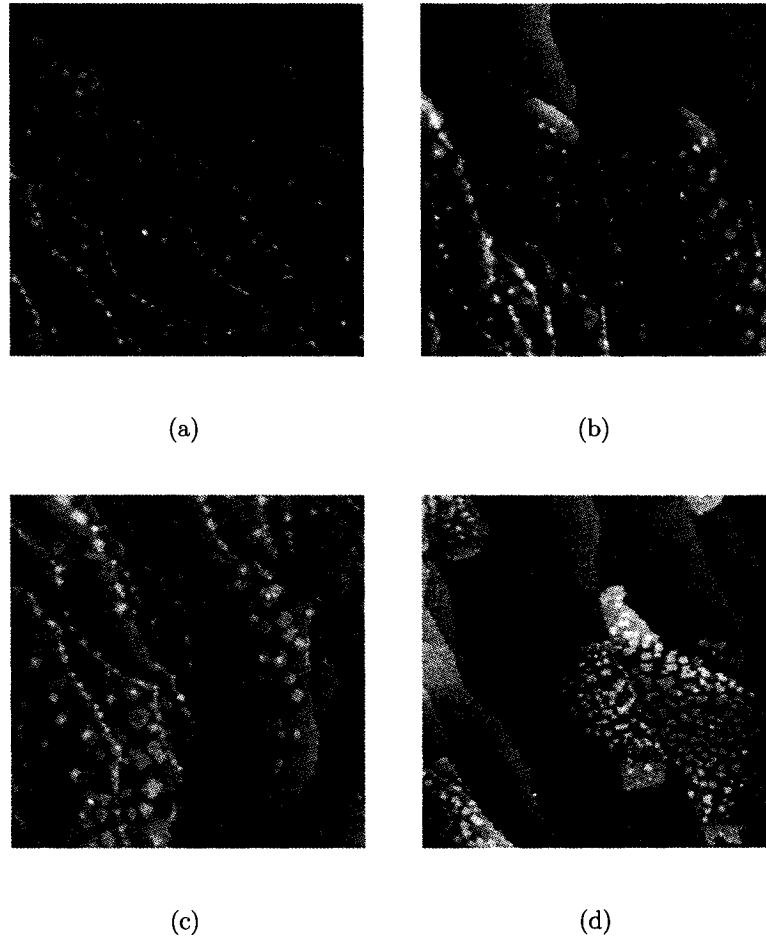


Figure 3.4: a), b), c) and d): non-contact AFM, topography, $500 \times 500 \text{ nm}^2$. The topography images reveal the growth mode of NaCl on copper. The first monolayer grows in a large island (film) while the subsequent monolayers grow in square islands on top of the film.

of NaCl ends on the copper terrace (as opposed to at a copper step edge), the islands density and size decrease as the distance to the edge of the salt film is reduced. All these observations will be discussed more deeply in the following sections. Note that the images shown are frames where NaCl was present. Most of the time the imaged exhibited only a bare Cu surface. Those images were not used.

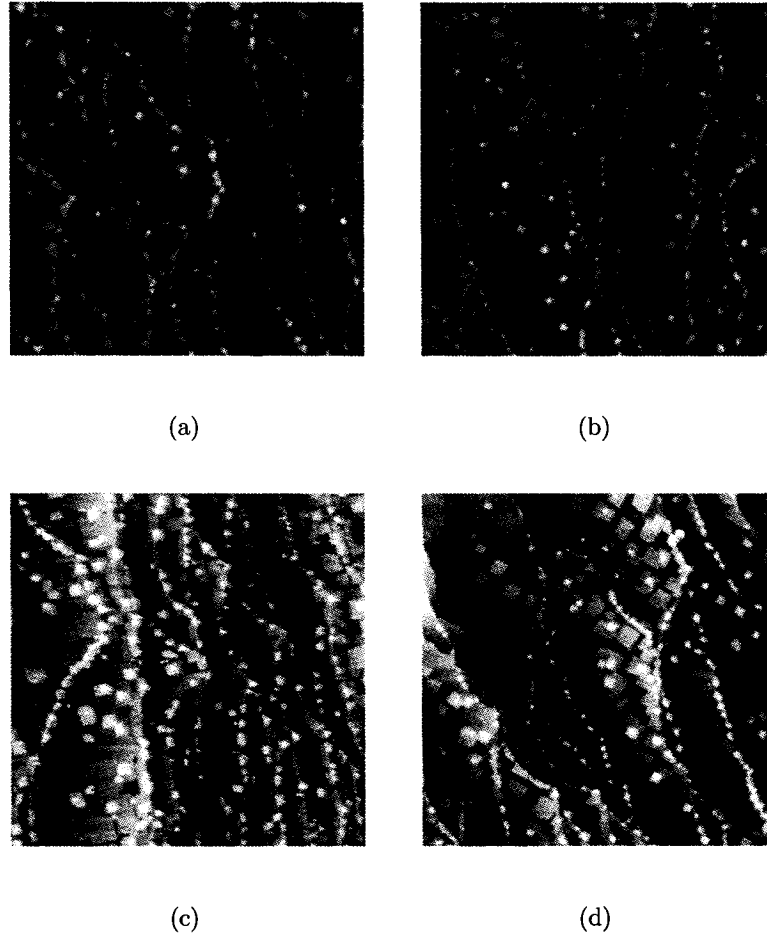


Figure 3.5: a), b), c) and d): non-contact AFM, topography, $500 \times 500 \text{ nm}^2$. A large amount of small islands grow over the edge of the copper steps while larger islands grow towards the middle of the terrace. A larger number of third monolayer islands grow near (over) the copper step.

3.2.2 Stranski-Krastanov growth mode

As underlined before, the growth mode of NaCl on Cu(100) is the Stranski-Krastanov mode. The fact that is used to distinguish the Stranski-Krastanov mode from the Frank-van der Merwe mode here is that the formation of the third monolayer starts *before* the completion of the second monolayer. In fact in figure 3.5(a) and 3.5(c) one can even see that some fourth monolayers islands are present without the second and third monolayer being completed. Figure 3.5 shows three images where the

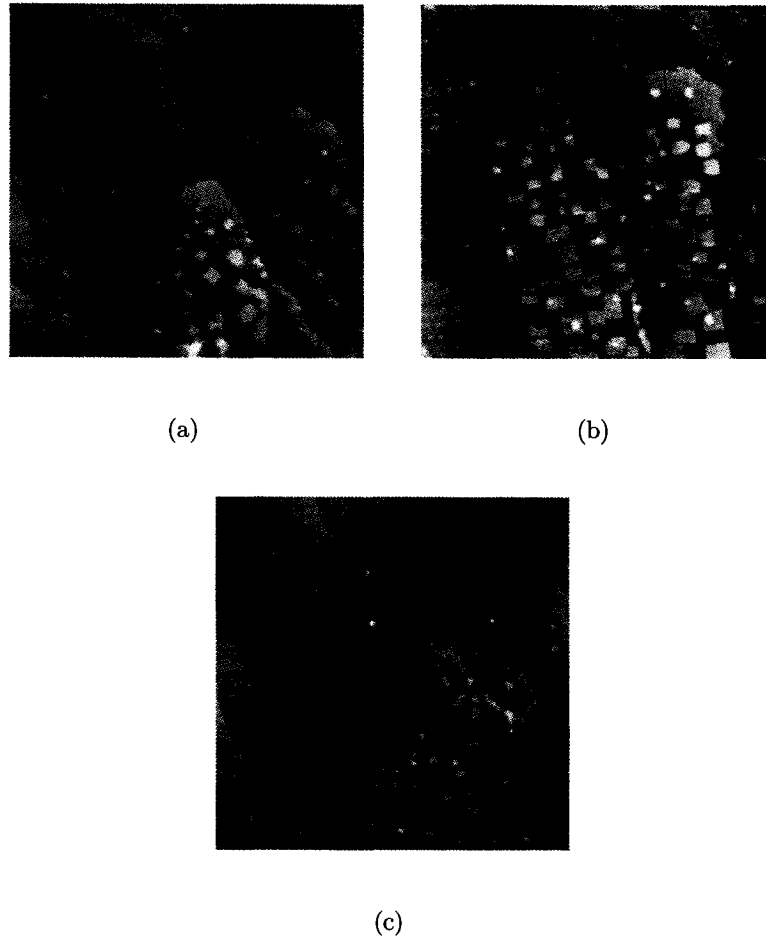


Figure 3.6: a), b) and c): non-contact AFM, topography. a): $400 \times 400 \text{ nm}^2$, b): $250 \times 250 \text{ nm}^2$, c): $225 \times 225 \text{ nm}^2$. The density of islands decreases towards the end of the film. Their size is also reduced compared with islands that grow farther from the edge of the film. The straighter edge of the salt film in c) is due to the deposition of the salt at a slightly elevated substrate temperature (353°K), hence the mobility of the NaCl molecules on the copper was increased.

imaged frame is covered in salt (no copper visible in figure 3.5(a) and 3.5(c) and very little copper visible in figure 3.5(b) and 3.5(d)). These images confirm the Stranski-Krastanov growth mode. As discussed in section 3.1.2, the Stranski-Krastanov growth mode implies that the heterosteps on the surface are non-reflective and that the homosteps are reflective. Thus the NaCl/Cu steps are non-reflective to NaCl adatoms

while the NaCl/NaCl steps are reflective to diffusing NaCl adatoms. Figure 3.4(d) shows that NaCl grows in large domains on the copper substrate indicating that the mobility of the NaCl molecules on the copper surface is high.

Note that to be completely sure that the growth mode is Stranski-Krastanov, one would need to evaporate more than one monolayer of film on the sample. This wasn't achieved in the present study. Although one can't be completely sure that the growth mode isn't Volmer-Weber, everything observed in the present study points to Stranski-Krastanov growth mode.

3.2.3 Shape and orientation of the NaCl islands

The second monolayer of NaCl grows on top of the first monolayer in well-oriented square islands of typical size of 20 nm to 50 nm. Such shape and orientation have already been observed on other systems, namely the growth of NaCl on Cu(111) [27, 28] (see section 3.3), Ge(100) [29], and Ge(111) [30]. Well-oriented epitaxial growth of thin films have also been observed by Kigushi *et al.* for various alkali halide on face-centered cubic (fcc) metal substrate [31] (see section 3.3). Subsequent monolayers also grow in square islands on top of the underlying layer keeping the same orientation from layer to layer. Figure 3.5(a) and 3.5(c) show topography images where third and even fourth monolayers are present and one can see that their shape has remained square and their orientation is the same as the underlying monolayer.

The NaCl crystal is a fcc crystal with a lattice constant a of 5.6 Å [12]. Hence its 2D unit cell is a square. It thus makes sense that the 2D NaCl islands growing on the NaCl film embrace a rectangular shape. In fact, the islands look more square than rectangular. This is because the density of impinging salt molecules on the surface is very homogeneous, hence no direction for the growth of islands is preferred (note that Yang and Flynn showed that NaCl impinges as a molecule and not as separate ions [32]). This shape also allows for kink and corner sites reduction. A rectangular (square) shape exhibits only four corner sites. Corner sites are energetically unfavor-

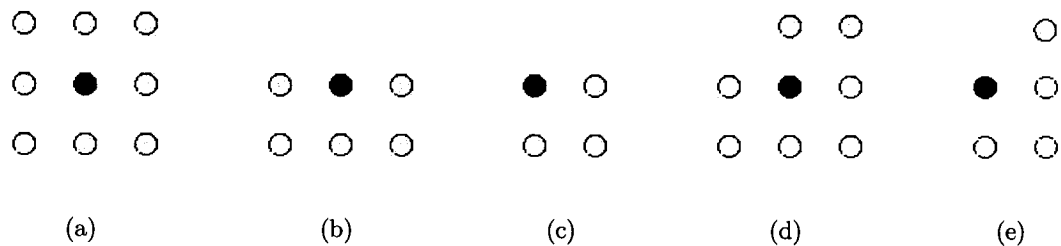


Figure 3.7: This sketch shows the neighbor and next-neighbor atoms (white dots) for an atom (black dot) at different location in an island. **a)** in the island itself the atom has four neighbors and four next-neighbors, **b)** at the edge of the island the atom has three neighbors and two next-neighbors, **c)** at a corner site the atom has two neighbors and one next-neighbor, **d)** in the corner of two merged island the atom has four neighbors and three next-neighbors, and **e)** at a kink site the atom has two neighbors and two next-neighbor

able as the molecules on these sites have less neighbors to bind with. This is also true for molecules on the edge of the islands which, in their case, have three neighbors to bind with. Bennewitz *et al.* showed that kink and edge molecules interact more with the AFM tip for NaCl on Cu(111) [33]. Figure 3.7 shows the neighbor molecules and next-neighbor molecules for an molecule at special sites in an island. Another reason why the square shape is favored over the rectangular shape is found when one considers the number of edge molecules. For an island of 100 molecules, there are four corner molecules for both the square and the rectangular shape, but the number of edge molecules is different. There would be 32 step molecules for a square island while there would be 42 step molecules for a 5×20 rectangular island. Thus the square shape is energetically favorable for the growth of NaCl on on the NaCl first monolayer. Another feature of the island shape exposed in the images of figure 3.5 is when two (or more) islands merge with each others. When two islands merge, it usually leads to the creation of two new sites where the molecules are missing one neighbor (unless the two islands are of the exact same size and that they merge in a perfect rectangular shape). These "new" sites are certainly less energetically unfavorable than corner sites and even edge sites as they are only missing on next-neighbor

molecule.

The relative orientation of the NaCl growth with respect to the Cu(100) substrate observed in this study are the two following: either NaCl(100) is rotated by 45° with respect to the substrate (100)-direction ($[100]_{\text{film}} / [110]_{\text{substrate}}$), or NaCl(100) is along the (100)-direction of the substrate ($[100]_{\text{film}} / [100]_{\text{substrate}}$). These two epitaxial orientations have already been observed on numerous systems as mentioned before. As Bennewitz *et al.* observed [28], the rotational domains have an inhomogeneous distribution over the surface. As it can be seen in figures 3.4, 3.5, and 3.6, only three out of eleven topography images show islands with 0° rotation. The reason could be that the growth orientation of NaCl is influenced by the direction of the underlying copper steps. It can be noticed that along $\{10\}$ -steps the NaCl grows along the $\{10\}$ -direction, and along $\{11\}$ -steps the NaCl grows along the $\{11\}$ -direction. This seem to be the case in all the topography images. One should note that the substrate orientation really refer to as general orientation. Thus, $\{10\}$ -steps are steps that run in the general $\{10\}$ -direction and similarly for $\{11\}$ -steps. Note that in the next section, it will be shown that these two types of steps are the only two possible on a fcc metal substrate. However one has to be careful with this hypothesis. The direction of the growth is "chosen" when the film starts growing. Thus the direction of the steps influence the direction of growth of the film only then. Even if the steps "change" direction somewhere along the film, this won't influence its growth direction has it was chosen at the beginning of the growth. Thus one can see some islands growing in the $\{10\}$ -direction along $\{11\}$ -steps an vice-versa, without refuting this hypothesis. Following this hypothesis, the fact that less 0° islands are present on the substrate is because there are less $\{11\}$ -steps on the surface, as it can be seen from the various topography images. In the next section, other step effects on the epitaxial growth of NaCl on Cu(100) are presented.

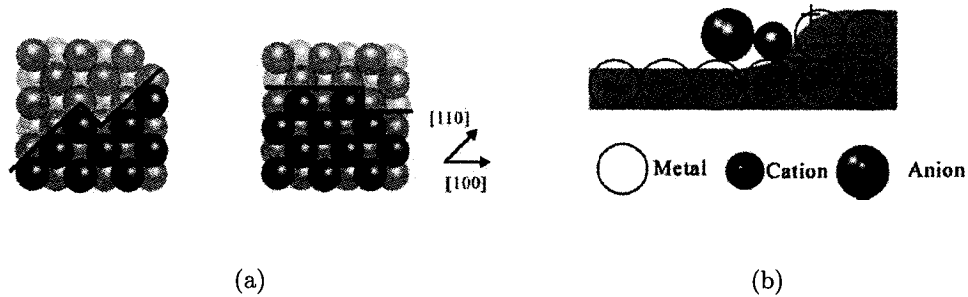


Figure 3.8: a) The two different step orientations on fcc (001) metallic surface with on the left a $\{10\}$ step and on the right a $\{11\}$ step b) The Smoluchowski effect at step edges. Because the lower side of the step edge is negatively charge, the cation of the alkali halide absorbs at the lower side of the step (from [31]).

3.2.4 Steps on a fcc metal and Smoluchowski effect

As shown in figure 3.8(a), the two types of steps expected to be found on a fcc transition (001) metal substrate are either in the $\{10\}$ -direction ($\{10\}$ -steps) or in the $\{11\}$ -direction ($\{11\}$ -steps). Other variation of steps can exist but they can be thought of combination of those two. The $\{11\}$ -steps exposes a (111) face while the $\{10\}$ -steps exposes a (100) face. While both types of step can be found on the surface, it has been showed that the (111) face is energetically more stable than the (100) face on the fcc transition metals [34], thus it is expected that the majority of steps on the surface will be $\{10\}$ -steps. In fact figure 2.13 on page 30 shows two STM images of the bare copper surface which confirm that the general direction of many steps is either $\{10\}$ -steps, $\{11\}$ -steps, or a combination of these two type of steps. However, even curved steps appear in some parts of the surface.

Another important effect at step edges as been introduced by Smoluchowski in 1941 [35]. He brought to the attention that the electron density perpendicular to the surface exhibits a relatively slow drop and that conduction electrons do not follow entirely the short-range corrugation of the surface. Thus the upper side of a step edge is positively charged while the lower side of the step edge is negatively charge (see

figure 3.2.4). The cation of the alkali halide molecules will preferentially absorb on the lower side of the step edge while the anion will preferentially absorb on the upper edge of the step [31]. Hence, the alkali halide molecules will preferentially absorb at step edges.

In fact it has been observed that the salt film start growing at the step edges. One can see this especially on figure 3.5(d) and 3.6(b). Even though these do not display the initial beginning of the growth of the film, they show the growth of the film on a "fresh" terrace. Thus one can speculate that initially the film starts to grow in a similar manner, hence it should start growing at the edge of a terrace. This is probably true in most cases and it has been shown that steps have good trapping properties for diffusing adatoms [25, 26]. In fact it has recently been shown that the nucleation of alkali halide films on the surface begins at step edges [36, 37]. One has to keep in mind that steps are not the exclusive trapping features of the surface. Other surface defects, such as impurities, can act as adatoms traps. However these are hard to identify as they either get covered by the NaCl film or get incorporated in the film as it grows all around it. Another important observation that was made about the film growth was that the edge of the underling copper steps are covered with small NaCl islands. These are an indication that the Smoluchowski effect has a important effect on film growth as it shows that the NaCl molecules are indeed attracted to the step edges. One can make a crude estimate of how much stronger the bonding between step edge and the molecules is stronger than the bonding between a flat terrace and the molecules by looking at the neighbors and nearest-neighbors in both cases. On a flat terrace, the molecule has one neighbor and two nearest-neighbors while at a step edge, the molecule has two neighbors and one nearest-neighbor. Hence, the bonding between a step edge and the molecules is stronger. The islands at step edges are smaller than their counterparts lying over the center of the copper terraces since the step edges attract the NaCl molecules and more nucleation sites are formed on the edges. Thus the nearby diffusing adatoms have more "choice" of sites where to bind to, resulting in more but smaller islands over the step edges.

3.2.5 The edge of the salt film

Figure 3.6 displays three typical images of the NaCl film ending on a copper terrace rather than at a copper step. These confirm that the size and density of the NaCl islands decrease near the end of the salt film. One can speculate on the mechanism for such a growth in this region of the film. First, it can simply be that just after the evaporation is stopped, there is still some salt molecules diffusing on the copper surface that eventually attach to the end of the salt film, making it grow further while the islands on top of it have already stopped growing since the mobility of NaCl on NaCl is low (hence the formation of islands). It can also be that the NaCl molecules can go down at the edge of the salt film and never come back up on the film, since the position at the end of the salt film is energetically more favorable as the salt molecule has more neighbors in that position than when it is diffusing on the salt film. Another possibility is that the edge of the salt film are reflective towards the salt molecules on top of it. This has already been discussed in section 3.1.2. In fact, during any Stranski-Krastanov epitaxial growth, as it is the case here, the heterosteps maybe non-reflective and the homosteps maybe reflective. This is confirmed by the fact that one can see the formation of third monolayer islands before the completion of the second monolayer. Hence the salt molecules (on top of the salt film) near the end of the salt film would have a tendency to be incorporated at the salt film step edge. This explains the smaller size and density of the salt islands near the end of the salt film. It is also quite possible that the reason why the edge of the salt film exhibits a less dense population of salt islands is a combination of these different phenomena.

3.3 Comparison with literature

A few scientific articles dealing with the growth of ultrathin films of NaCl on copper are available in the literature. Among which, Kiguchi *et al.* studied the growth of alkali halides on different fcc metal surfaces, Mauch *et al.* [19] presented the growth of NaCl on Cu(100), Fölsch *et al.* [38] studied the growth of NaCl on Cu(211), and Bennewitz *et al.* [27] presented the growth of NaCl on Cu(111).

Growth of alkali halides on fcc metal substrate

The growth of different alkali halide on fcc metal substrates has recently been studied by Kiguchi *et al.* [31] The studied systems were LiCl/Cu(001), LiCl/Ni(001), LiCl/Ag(001), NaCl/Cu(001), NaCl/Ag(001), and NaCl_{0.6}Br_{0.4}/Ag(001). Epitaxial growth of these halide films was studied by means of RHEED which, compared to SPM techniques, studies the film on a large scale. The growth of these halides has been performed for substrate temperature of 300°K and 420°K. Two types of epitaxial orientations were found, that is the alkali halides either grew with their (100)-direction rotated by 45° with respect to the (100)-direction of the substrate ($[100]_{\text{film}}/[110]_{\text{substrate}}$) or with no rotation ($[100]_{\text{film}}/[100]_{\text{substrate}}$). On the LiCl/Ag(001) system the two orientations were found, while on the other systems only one orientation was found. Since the chemical interaction between metals and alkali halides is weak, the bonding of the molecules to a terrace is weak. It is also known that the bonding between the step edge and the molecules is rather strong.

This brings useful insight to the current project. It in fact confirms that alkali halides preferably grow in the two observed directions. Specifically for the NaCl/Cu(100) system Kiguchi *et al.* found only one substrate orientation, which is NaCl(100) being parallel to the (100)-direction of the substrate (for epitaxial growth at a substrate temperature of 420°K). The growth temperature probably plays a role in the epitaxial film orientation as the surface diffusion of adatoms is increased for increased substrate temperature. Another possibility is that as mentioned earlier, the growth orientation of the different domains is not homogeneous over the substrate surface. Thus it could be that the studied part of the sample had a enormous concentration of domains oriented along the (100)-direction of the substrate. Although possible, this is not likely to be the case as even with a lower concentration of domains oriented along the (110)-direction of the substrate, the RHEED spots would have been dimmer, but most likely visible, hence the direction could probably have been identified for epitaxial growth. For the growth at room temperature (substrate temperature of 300°K), the growth of a polycrystalline film was observed. This maybe because the

deposited NaCl film thickness was higher in this experiment. The orientation of the film after the deposition of many monolayers is may not be in registration anymore with the underlying substrate. Thus the steps of the substrate are expected to be important for the growth of alkali halides on metals.

Growth of NaCl on Cu(100)

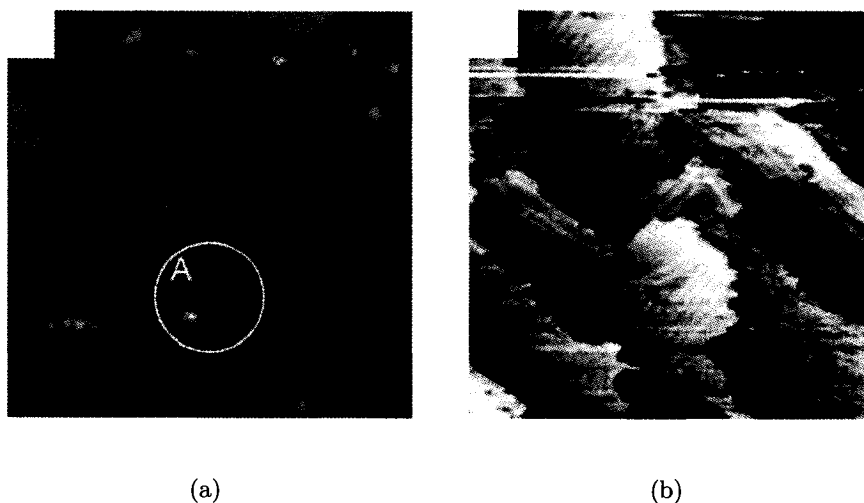


Figure 3.9: STM images, a) $730 \times 730 \text{ \AA}^2$ and b) $800 \times 800 \text{ \AA}^2$. a) The formation of NaCl stripes on Cu(100) induce the restructuring of the Cu(100) along the direction on the stripes. In the circled area A, one can see that where perpendicular stripes merge with the terrace, the terrace boundary is more irregularly shaped. The local stripes coverage varies a lot as it can be seen by comparing images a) and b) (from [19]).

The paper by Mauch *et al.* is of particular interest because it deals with the exact same interface as the the system studied in this project and it is studied at a similar scale. A coverage of 0.2 monolayer and 0.7 monolayer of salt have been deposited on the copper substrate, with the substrate being at room temperature during the deposition, at a growth rate of about 0.5 to 1 \AA per minute and the system was studied by STM and LEED. For the 0.2 monolayer coverage, islands were observed and were believed to be copper islands (from a height analysis). The explanation

for the presence of such islands is that the diffusing copper atoms on the surface probably nucleate in the presence of NaCl molecules. For the 0.7 monolayer coverage, the observation of straight stripes that never join or touch with a height of about 0.5 \AA aligned in the $[011]$ and $[01\bar{1}]$ directions was made. Also, the NaCl stripes seem to induce the restructuration of the Cu(100) terraces along the same direction as the stripes (see figure 3.9).

Clearly, there is an enormous difference between the observations made in this project and the one made by Mauch *et al.* Despite similar conditions for the epitaxial growth of NaCl on the Cu(100) substrate, the observation of NaCl stripes was never achieved. Careful and repeated studies of the deposition of ultrathin NaCl films on a Cu(100) substrate always revealed the same growth mode, that is Stranski-Krastanov growth with the NaCl film, with well oriented, square islands, the (100)-direction of the NaCl film being oriented either along the copper (100)-direction or its (110)-direction. The major differences between the two studies were the growth rate of NaCl (although the film thicknesses are similar) and the probe used to study the surface. In Mauch's study a STM was used while in the presented project, non-contact AFM was used.

Growth of NaCl on Cu(211)

Fölsch *et al.* studied the growth of NaCl on a Cu(211) surface [38]. The interface NaCl/Cu(211) has been studied using high-resolution low-energy electron diffraction (SPALED) and low-temperature STM (all images were recorded at 13°K). The bare Cu(211) surface is a vicinal surface consisting of (111) terraces and intrinsic (100) single steps which run along the $[01\bar{1}]$ in-plane direction [38]. The deposition of NaCl at a substrate temperature of 370°K induce a surface restructuration of the copper surface as shown in figure 3.10. One NaCl monolayer selectively grows on the (311) facet of the surface as confirmed by comparing the surface area of the (311) facet with the amount of deposited material. The surface restructuration of the copper is complete when the surface exhibits a coherent array of NaCl-covered (311) facet

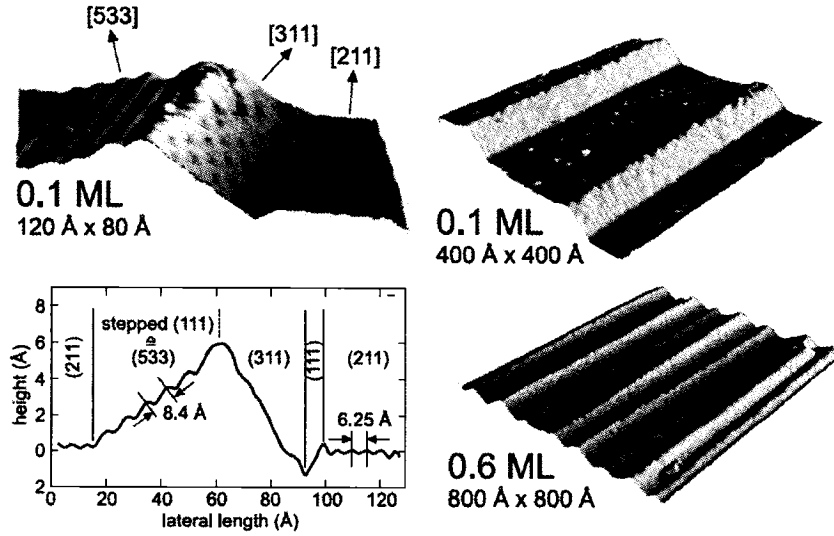


Figure 3.10: The growth of NaCl on Cu(211) at a substrate temperature of 370°K induce a surface restructuration as shown in the three STM images. The NaCl selectively grows on the ascending Cu(311) (inclined by 80°) face which is compensated by a regularly stepped Cu(111) (inclined by 70.5°) descending face with the step of this descending facet being separated by $\sim 8.4 \text{ \AA}$ (equivalent to a (533) orientation inclined by 5°). Note that all the angles are given with respect to the macroscopic surface normal. The graph shows a scan line (profile) perpendicular to the intrinsic steps which schematize this restructuration taken from the 0.1 ML coverage image. Note that only the Cu atoms are displayed on this graph (from [38]). The 0.6 ML coverage image shows that the restructuration of the copper surface is completed at that coverage.

and (111) facet of copper. This happens at a surface coverage of ~ 0.6 monolayer. The uniform 2D layer growth of NaCl on the (311) facet shows that this epitaxial orientation is energetically favorable. In fact, SPALEED analysis showed similar lattice spacing for the Cu(311) face and the covering NaCl. In a later study, the same group showed that it is actually the Smoluchowski effect which is responsible for the strong interaction between Cu(311) and the NaCl film. [39]

There is a striking difference between the observations made by Fölsch *et al.* or the epitaxial growth of NaCl on Cu(211) and the one made in this project for the epitaxial growth of NaCl on Cu(100). This is most likely due to the substrate which, despite being the same material, exhibits a different face of the copper. However, one important conclusion links the two studies. There is undoubtedly an interaction between the film and the substrate. In the study made by Fölsch *et al.* the deposition of the film triggers a surface restructuring, while in the presented project this interaction is observed via the fact that the film grows in registry with the substrate.

Growth of NaCl on Cu(111)

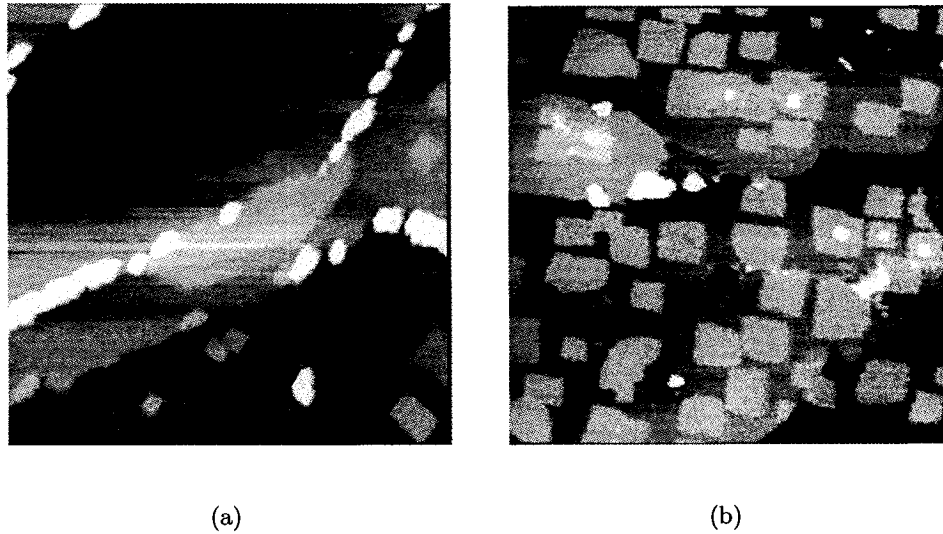


Figure 3.11: Non-contact images of NaCl ultrathin films on a Cu(111) substrate. a) $263 \times 263 \text{ nm}^2$ and b) $370 \times 370 \text{ nm}^2$ (from [27]).

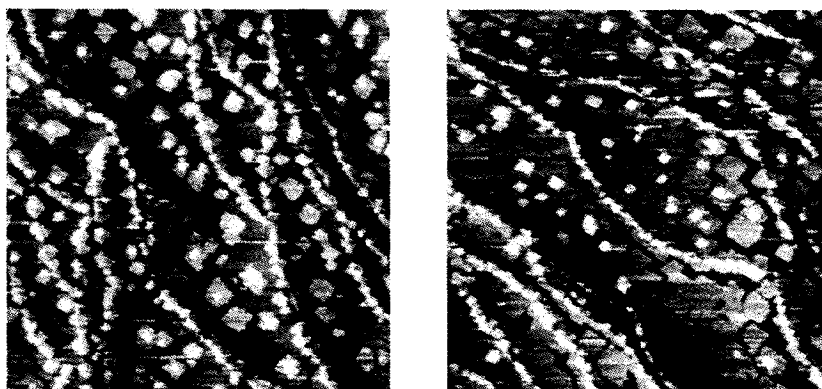
Bennewitz *et al.* have studied the NaCl/Cu(111) system using both dynamic force microscopy (DFM) and LEED [27, 28]. They have observed that the deposited NaCl first form a large film and then, the second monolayer starts to grow well-oriented rectangular island (figure 3.11). Atomic resolution on the NaCl first and second monolayer of salt was achieved revealing the periodicity of the NaCl. DFM topography images and LEED revealed three possible orientations for the cubic NaCl films along

a specific (110)-direction on the Cu(111) surface which are the films being rotated by either 0° , 60° , or 120° . A contraction of the NaCl film of $\sim 3\%$ compared with the bulk lattice constant was also observed. A similar observation of contraction of the lattice constant for NaCl deposited on Al was also found by Hebenstreit *et al.* [40] indicating that the contraction of the lattice is an inherent feature of ultrathin NaCl films [28]. In the present case it resulted in the growth of the film in a preferred orientation with respect to the Cu(111) surface.

The observed orientations for the growth of the NaCl films presented in section 3.2 are in agreement with the results presented by Bennowitz *et al.* For the growth of ultrathin films of NaCl on Cu(100) two preferred orientations were observed and the fact that the NaCl thin films grow in preferred registry with the underlying substrate indicates that the lattice of the NaCl film adjusts to the substrate. A LEED study would have to be performed to verify that assessment.

Chapter 4

Friction on NaCl/Cu(100)



(a) april1-m24, 500nm

(b) april2-m1, 500nm

Figure 4.1: a) and b): Contact AFM, topography, $500 \times 500 \text{ nm}^2$. Overviews showing an area where the NaCl film completely covers the copper substrate.

This experiment is designed to perform friction force measurements on the different monolayers of NaCl deposited on a Cu(100) substrate, particularly to study the difference in friction between the first and second monolayer of NaCl. Thermal evaporation of NaCl has been performed under UHV conditions using the built-in evaporator (see section 2.5). First, contact AFM images of the surface are presented and discussed in section 4.1. The coverage of the surface for this experiment has been estimated to be $2/3$ of a monolayer. Note that the presented images were recorded

at specific position on the sample and are not the typical image one would get by approaching and imaging the first frame. Most of the sample surface exhibits bare copper and the focus was made on recording the frames where NaCl was present. The increased coverage compared with the previous experiment (see chapter 3) has been chosen to overcome the difficulty of imaging two different materials in contact mode. This will be discussed in section 4.2. The friction on the different monolayers is discussed in section 4.3. Also stick-slip measurements on NaCl were performed and are presented in section 4.4. Finally, a comparison with literature for friction of thin films of alkali halide deposited on a metal substrate is made in section 4.5.

4.1 Contact AFM measurements on NaCl-Cu(100)

First, contact AFM images have been taken to verify that the system is similar to what has been observed with the AFM in non-contact mode (figure 3.4 on page 43). The images presented in figure 4.1 both display the observed characteristics of ultrathin films of salt on copper: the salt grows in a Stranski-Krastanov mode, the islands exhibit a square shape, and the edges of the underlying copper steps are decorated with many small islands. In both images, the salt fully covers the copper surface. Hence, the observed system is the same as what has been observed with non-contact AFM and provides an excellent candidate for the measurements of friction on different monolayers of NaCl.

In an attempt to investigate the friction contrast between different monolayers of NaCl, contact AFM images showing only few islands were acquired. The typical island size being of the order of 20 nm to 50 nm, images of the size of about $100 \times 100 \text{ nm}^2$ should display only a few salt islands. Figure 4.2 shows four contact images of that type. One can notice that the islands shape is not perfectly square in all the images. In contact measurements, the tip shape has a great influence on the recorded topography images and hence, it can be that the tip was not very sharp when these images were recorded. Another factor is that the salt molecules may have been displaced by the

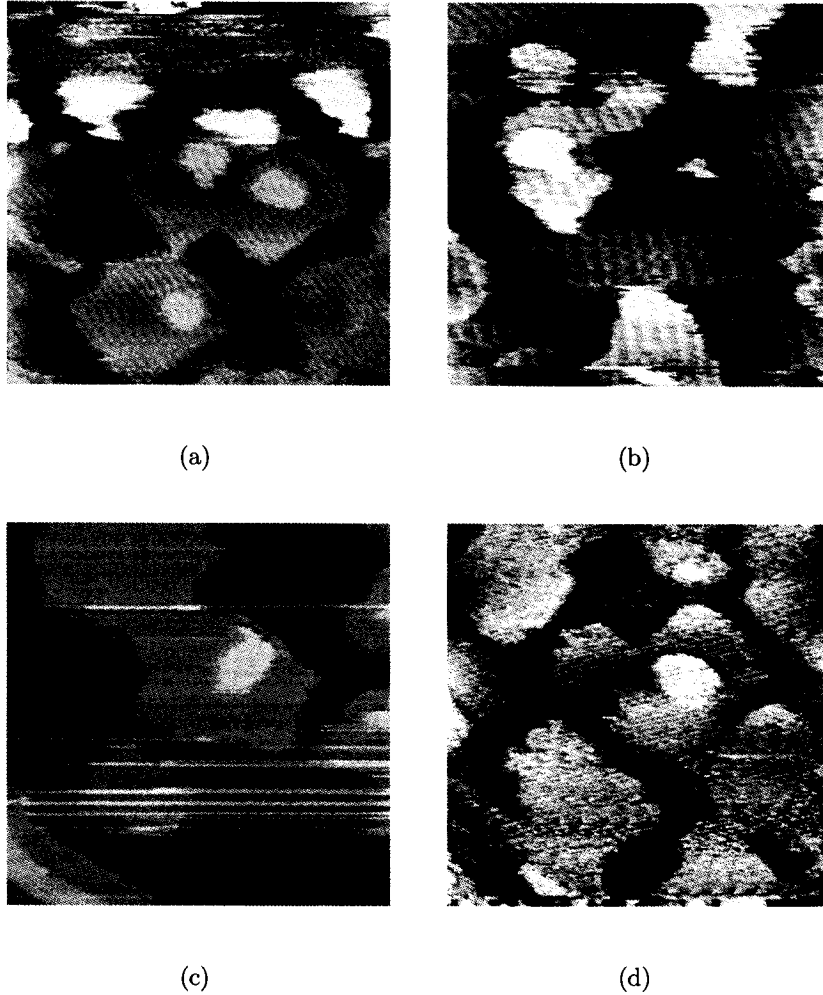


Figure 4.2: **a)**, **b)** and **c)**: Contact AFM, topography, $100 \times 100 \text{ nm}^2$. **d)**: Contact AFM, topography, $125 \times 125 \text{ nm}^2$. NaCl islands in contact mode. The 20 Hz building noise is visible particularly in **a)**, **b)** and **c)**.

tip during the measurement, hence changing the shape of the islands. Along with topography, the forward and backward lateral forces (F_L) have been recorded. These combined with the topography can be used to analyze the friction contrast between the different layers. Next, the difficulty to image the surface when two different materials are present in the same frame will be address.

4.2 Difficulties to image two materials in contact mode

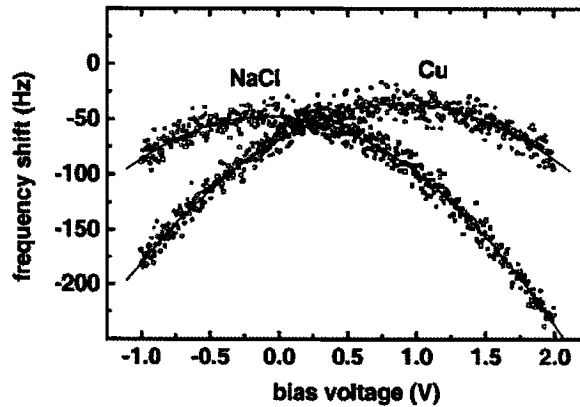


Figure 4.3: Measurement of the bias voltage versus the frequency shift as measured on the bare copper substrate and on the NaCl film (from [27]).

The electrostatic forces between the tip and sample can be compensated by applying a proper bias voltage for the different materials [27]. Bennewitz *et al.* have recorded the variation of the frequency shift of a cantilever at a fixed distance from the surface with respect to the bias voltage (the minimum of the frequency shift happens when the difference in contact potential between the tip and the sample is compensated by the bias voltage). When the bias voltage compensates for this difference in work function, the electrostatic force vanishes. It was found that the bias voltage required to compensate the electrostatic force on NaCl is 1 V below the value required for copper (bias voltage of ~ 1.0 V for copper and ~ 0.0 V for NaCl. [27])

When imaging a surface (using an AFM) with two different species present on the surface, one cannot minimize the electrostatic force for both species. Hence the difficulty to obtain a good topography image when both materials are present in the scanned frame. As Bennewitz *et al.* demonstrated, the bias voltages required to compensate the electrostatic force on NaCl and on copper are different, thus imaging

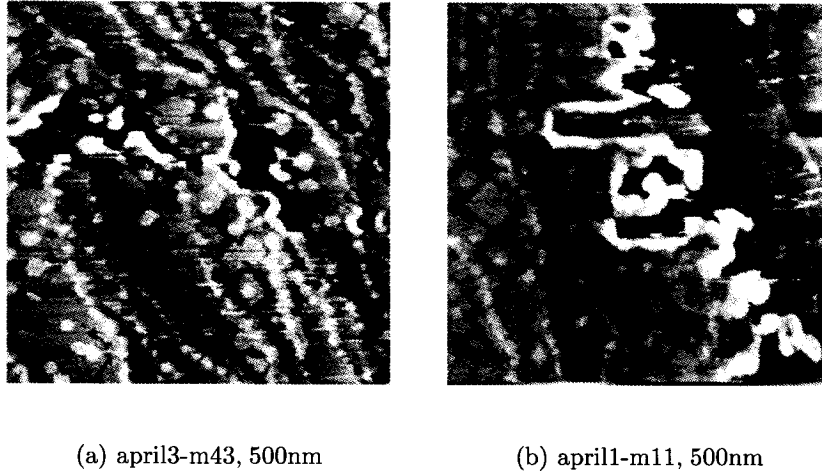
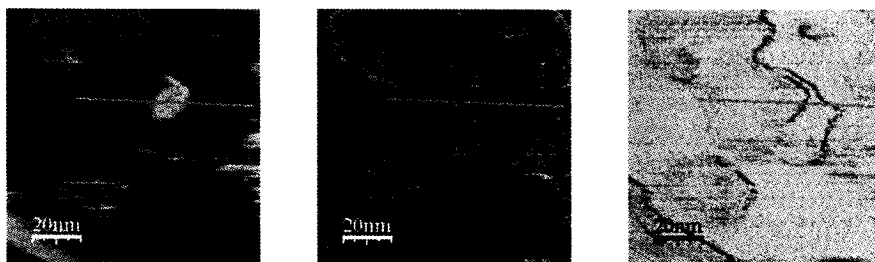


Figure 4.4: **a)** and **b)**: Contact AFM, topography, $500 \times 500 \text{ nm}^2$. Overview showing the NaCl film with copper present. These images are hard to acquire because of the different electrostatic potential between the two materials.

both species in contact mode is difficult. In figure 4.4(b) the bias voltage was set to minimize the electrostatic force on copper, while in figure 4.4(a) the bias voltage was set to minimize the electrostatic force on NaCl. The electrostatic force was minimized by first using the value found by Bennewitz *et al.* and then adjusting it until the best contrast was reached. Note that Bennewitz *et al.* underlined that contact AFM imaging of Cu(100) was very difficult to obtain. [41]

4.3 Friction contrast

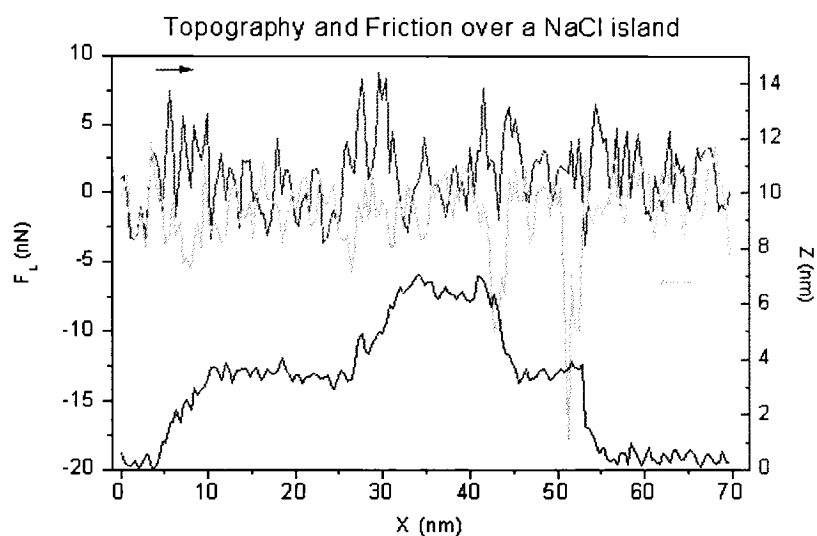
Figures 4.5(a), 4.5(b) and 4.5(c) display the topography, and the forward and backward lateral forces along with a common profile for the three images. The data from the profile for the three images is then plotted in figure 4.5(d). This is a typical result of friction contrast over the different monolayer of salt and it has been reproduced numerous times over different islands at different positions on the surface. Clearly, the friction contrast between the different layers of the salt can't be determined to be either greater, less or the same as the signal-to-noise ratio is very poor. However, the friction contrast measurements seem to indicate that the friction increases at the



(a)

(b)

(c)



(d)

Figure 4.5: a), b) and c): Contact AFM, $100 \times 100 \text{ nm}^2$, topography, forward lateral force and backward lateral force. d) The friction and the height along the profile. Although no friction contrast between the different monolayers of NaCl can be distinguished, the friction is clearly greater at the edges of the different layers.

edges of the different layers. One has to note that this measurement (along with all the others) has been performed at a very low load (-10 nN). It can be that a contrast between the different layers would be observed at higher loads, as the lateral force increases with load. However, imaging at higher loads can become problematic as the tip could *scratch* the surface and move the salt molecules around on the surface. Thus,

when trying to image at higher loads, one has to be extremely careful and increase the load very slightly between each scans. This could not be performed during this experiment as the tip-sample system was very unstable with the tip either jumping off the surface or crashing on the surface during the recording of the first or second scan. Hence, sometimes a somewhat good quality image could be recorded (figure 4.2(b), 4.2(c) and 4.2(d)) and sometimes only part of an image could be recorded (figure 4.2(a)). The presented result for the friction contrast is very reproducible over the presented image.

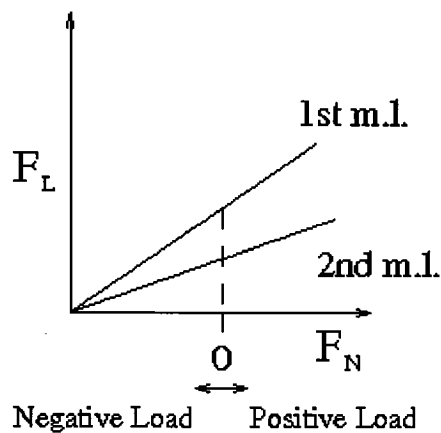


Figure 4.6: A schematic diagram of the lateral force (friction) versus the normal force. The point of zero load is shown. The negative load region is when the applied load is negative, meaning that one is pulling on the cantilever to compensate adhesion. The positive load region means that the applied load is positive, hence one is pushing the cantilever on the surface. Note that the adhesion between the tip and the NaCl layer can be different for the first and second monolayers. Even if this is the case, the general idea of the graph is the same, the two curves simply having different origins.

Figure 4.6 shows a schematic plot of the lateral force versus the normal force at low loads. One has to note that the curves might not look like straight lines at these loads and that this is just to show the expected difference in the friction between the first and second monolayer of NaCl. The friction contrast shown in figure 4.5 was recorded at -10 nN. Thus one can see that at such load, a possible friction difference

between the two monolayers would be rather small hence very difficult to distinguish from the noise in the signal. At higher loads the separation between the two curves is expected to increase allowing for a better signal to noise ratio in the friction contrast.

4.4 Stick-slip over a NaCl island

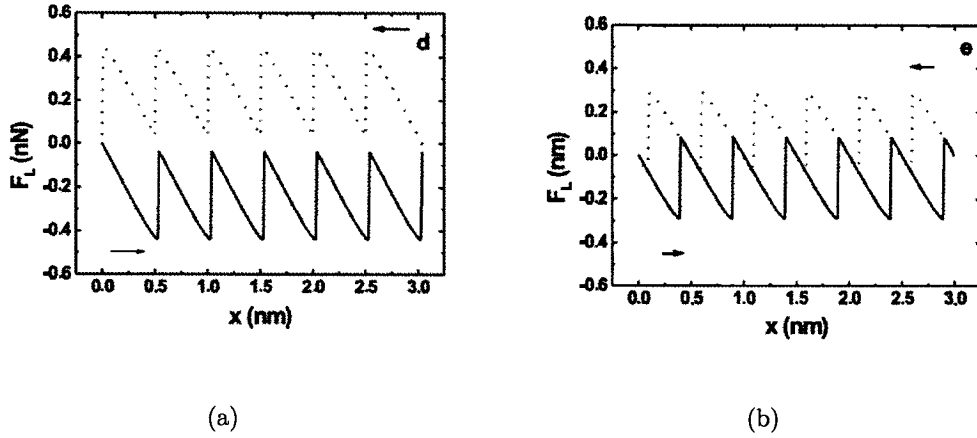


Figure 4.7: Tomlinson simulation of atomic-scale stick-slip for two different loads, the load in **a**) being greater than the load in **b**) (from [42]).

The measurement of the lateral force can reveal the atomic structure of the material under study. Under certain conditions, the measurement of the lateral force can lead to the observation of a sawtooth-like behavior which is in accordance with the periodicity of the lattice of the studied surface. This is called atomic stick-slip and it first has been observed by Mate *et al.* [43] by sliding a tungsten tip over a graphite surface and recording the lateral force with a FFM. The stick-slip behavior of the lateral force revealed the honeycomb structure of the graphite surface. The Tomlinson model has been proposed for this molecular friction by Tománek *et al.* [44] In a stick-slip experiment, the tip is scanned over the periodic potential defined by the atomic structure of the surface and the contact [42]. In this case, the cantilever-tip system can be described as a spring holding the tip and this is what records the lateral force. When the tip encounters an atom on the surface, it sticks to it until

the pulling force exerted from the cantilever is strong enough to make it jump to the next atomic position (slips). Numerical simulation from the Tomlinson model are presented in figure 4.7. These simulations assumed that the tip is scanned over a sinusoidal potential, with the spring constant being a combination of the stiffness of the cantilever and the lateral stiffness of the contact. [4, 42]

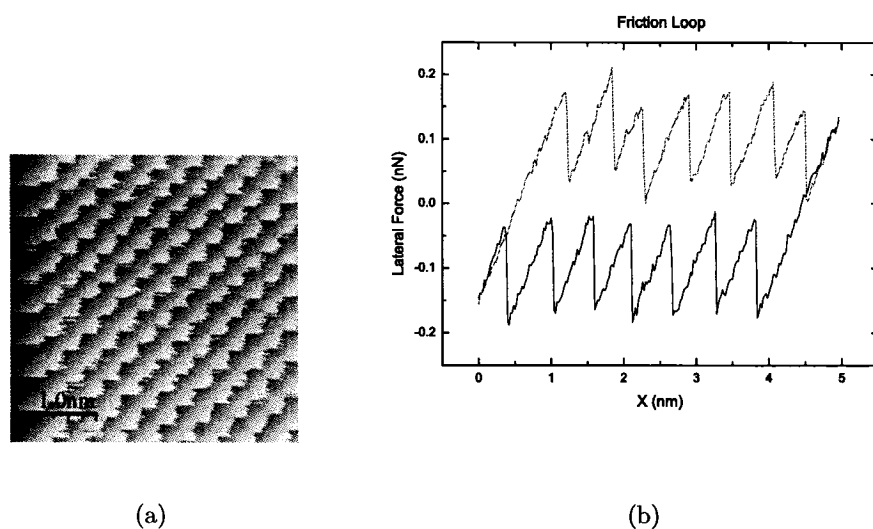


Figure 4.8: **a)** Typical stick-slip measurement over a 45° island performed at a load of 0.2 nN and a scanning velocity of 20 nm/s. The scan has been performed at an angle of 45° with respect to the origin in order to exhibit the lattice constant of NaCl. **b)** A typical scan line from the stick-slip image. From this graph the lattice constant of NaCl has been estimated to be 0.55 ± 0.10 nm. The force calibration is approximate only since the scan is performed at a 45° angle.

Stick-slip measurements as described in the preceding paragraph have been performed over an NaCl island. Figure 4.8(a) shows the acquired image under these conditions. A profile taken from the image is shown in figure 4.8(b). This clearly exhibit a stick-slip pattern. This has been recorded on a 45° NaCl island, with the scanning angle from the tip being also 45° in order to scan along the (100)-direction of the NaCl. As mentioned before, the observed sawtooth in stick-slip is in accor-

dance with the periodicity of the lattice of the studied surface. Since one stick-slip event corresponds to one molecule, one can determine the periodicity of the lattice by simply subtracting the distance between two events. In figure 4.8, the periodicity of the lattice has been determined to be 0.55 ± 0.10 nm. The reason for such a high error ($\sim 18\%$ of the measured value) is that, as specified in section 2.3 on page 24, the calibration of the used AFM in the x -direction hasn't yet fully been established. The expected scanning range has been calculated and the fact that the measured lattice constant of the salt is in accordance with the crystallographic value which is 0.56 nm [12], this confirms that the calculated scanning range is very close to what it should be.

4.5 Comparison with literature

The frictional properties of thin halide films

The frictional properties of thin halide films deposited on a metallic substrate have been studied by Gao *et al.* [45, 46, 47] Thin films of KCl, NaCl, FeCl₂ and KI deposited on iron were studied using a tribometer pin with a tungsten carbide ball in an UHV environment. Basically, the pin is run across the surface and measures the friction coefficient. The friction coefficient of iron is known to be ~ 2 . The deposition of ~ 40 Å of KCl, ~ 30 Å of FeCl₂, ~ 50 Å of NaCl and ~ 40 Å of KI on a fresh iron surface resulted in the minimization of the friction coefficient (each film of halide is deposited on a freshly prepared iron surface and then the friction coefficient is measured). At the specified thickness, the friction coefficient as been measured to be ~ 0.27 , ~ 0.55 , ~ 0.08 , and ~ 0.23 for the KCl, NaCl, FeCl₂ and KI films respectively (figure 4.9 shows the friction coefficient versus the thickness for KCl and NaCl). It was demonstrated that the minimization of the friction coefficient corresponds with the completion of the first monolayer of the halide film. One shall note that the second - and often subsequent - monolayer starts to grow before the first monolayer completely covers the surface, hence the measured thickness for the minimization of the friction coefficient is greater than the thickness for one monolayer of the deposited

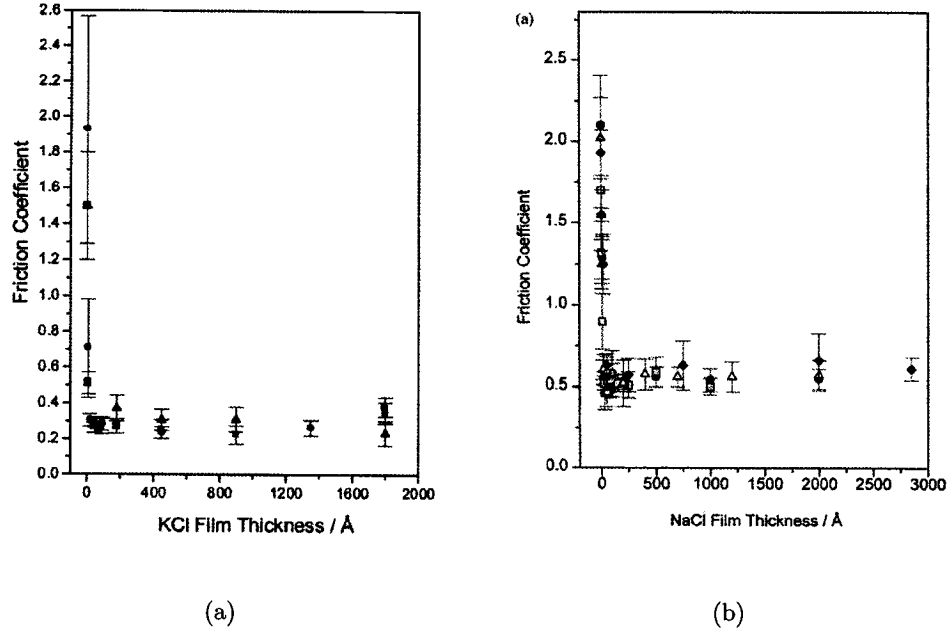


Figure 4.9: The friction coefficient of alkali halides versus the deposited film thickness measured on iron. a) KCl (from [45]) and b) NaCl (from [46]). The different shapes represent different experiments showing the reproducibility of the experiment.

halide film. Mathematically, this can be modeled as (assuming that the adsorption kinetics into the first and subsequent layers are identical)

$$\mu - \mu_{\text{film}}^0 = (\mu_{\text{Fe}}^0 - \mu_{\text{film}}^0) e^{-\alpha t} \quad (4.1)$$

where μ is the friction coefficient, μ_{film}^0 is the limiting friction coefficient of the film, μ_{Fe}^0 is the friction coefficient of the clean iron substrate, t is the thickness of the film, and α is equal to $\frac{1}{t_0}$, where t_0 is the thickness of the first monolayer of the film. [45, 46, 47]

The experiments performed by Gao *et al.* are of particular interest as they study frictional properties of systems similar to the NaCl/Cu(100) system. Albeit on a larger scale, these experiments provide useful information about the friction in systems of halide films on metallic substrate. Using a modified equation for the friction coefficient with the values for copper (i.e. replacing the friction coefficient for the

clean iron substrate by the one for copper) and knowing the limiting value of the friction coefficient for NaCl on copper, one can find the coefficient of friction for a NaCl film on copper. Another striking result from the Gao *et al.* experiment is that the friction coefficient is reduced to its minimal value after the completion of the first monolayer only. Hence relating to the friction contrast experiment between the first and second monolayer, that would imply that the friction should not be reduced between the two different monolayers. Though, one shall keep in mind that the experiment by Gao *et al.* is performed on a relatively larger scale and that the probe used to measure the friction coefficient might not be as sensitive to small scale variation in the friction coefficient. In the friction contrast experiment, the tip of a cantilever is used which is of a typical size of ~ 10 nm, while the tribopin used in the friction coefficient experiment is of a size of ~ 6 mm. Also, this experiment was done at relatively high loads, ~ 1 N, while a typical friction experiment using a FFM is performed on loads of the order of ~ 1 nN, if not even in the negative nN force regime. Thus, even though the friction contrast was found to be similar on both monolayers which is in accordance with the Gao *et al.* experiment, the friction contrast between different monolayers is worth further investigations, in particular by reducing the noise, to properly verify that the friction between the different monolayers is either different or the same on the nanoscale.

Stick-slip on NaCl(100)

Since the birth of the FFM, many stick-slip studies on different materials have been performed. The focus here will thus be made on stick-slip studies on NaCl. Gnecco *et al.* [48] studied the velocity dependence of atomic friction using a NaCl(100) crystalline surface. Event though the velocity dependence of atomic friction is not of so much interest for the presented stick-slip (section 4.4), some interesting results are presented. Figure 4.10 shows a lateral force image and a friction loop as measured on a NaCl(100) crystalline surface. It exhibits a similar sawtooth pattern to what has been observed in figure 4.8. The main difference between the two measurements is the load applied and the lateral force obtained in the curves. On the friction loop in

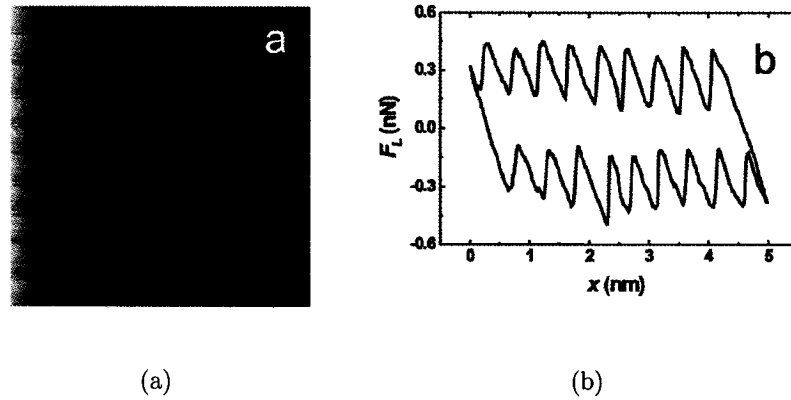


Figure 4.10: Stick-slip measurements on NaCl(100), $5 \times 5 \text{ nm}^2$ (from [48]) a) Lateral force image at a 0.65 nN load and at a scanning velocity of 25 n/s b) Friction loop taken from a profile on the lateral force image.

figure 4.8(b) one can see that the lateral force has a range of about 0.4 nN whereas in the friction loop in figure 4.10(b), the range of the lateral force is about 0.9 nN. A lower lateral force is expected as the stick-slip process in figure 4.8 was recorded at a lower load and at a smaller scanning velocity than the one recorded by Gnecco *et al.* The fact that the peaks are not all at a constant height (fluctuation of the maximum lateral force) arises from thermal fluctuations as shown by Sang *et al.* [49]

Chapter 5

Conclusion

An UHV-compatible molecular beam evaporator has successfully been built. The deposition of NaCl on a copper surface was confirmed by means of Auger spectroscopy, non-contact AFM and contact AFM. The growth rate has been evaluated to be ~ 1 monolayer per hour, which compared to commercial evaporators is rather low, but permits a greater control on submonolayer deposition. Furthermore, the growth mode of NaCl on Cu(100) was studied using non-contact AFM. It was determined that NaCl grows in a Stranski-Krastanov mode, with the first monolayer of salt growing over copper in a large island and lying over the copper steps in a carpet-like way. The second and subsequent monolayers grow in well-oriented square islands on top of the previous layer. The NaCl film was found to grow in registry with the underlying copper substrate with the (100)-direction of the film growing along either the (110)- or the (100)-direction of the copper substrate. The result obtained by Mauch *et al.* [19] could never be reproduced even though similar growth conditions were used. The obtained results for the growth mode are in accordance with the results obtained for a similar system (NaCl/Cu(111)) studied by Bennewitz *et al.* [27] The friction contrast between the first and second monolayer of NaCl was studied using a FFM. The difference in friction between the different layers couldn't be measured within the noise. It is possible that this difference exists at higher load. This would require further investigations. Along with the pursue of a better signal-to-noise ratio to investigate the frictional properties between different monolayers, other experiments could be

performed to gain further knowledge in the subjects presented in this project. Annealing the evaporated film and then imaging the surface would foster the equilibrium growth mode of NaCl on Cu(100). Also LEED studies of submonolayer growth would reveal the lattice constant of the first (and most likely second) monolayer indicating if the film is contracted. One could also "scratch" the salt film with an AFM tip and study the wear and defects produced. The latter could also be used to study surface diffusion of NaCl molecules on the copper surface.

Appendix A

UHV System

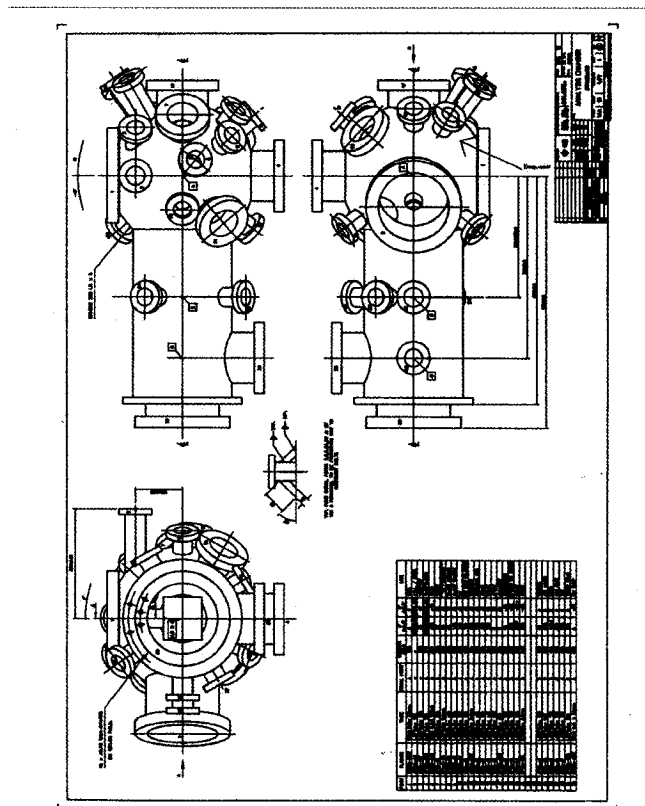


Figure A.1: A technical drawing of the UHV system from Omicron [15]. An arrow in the top right corner shows where the evaporator was installed.

Appendix B

Auger Electron Spectroscopy

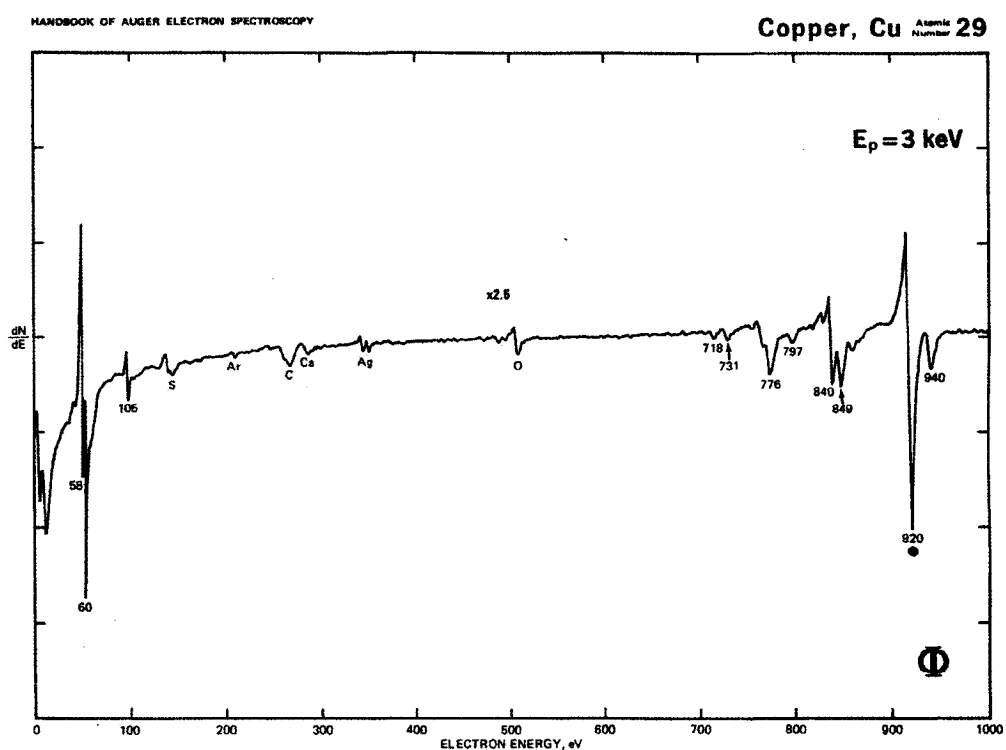


Figure B.1: Auger spectrum of copper from [11].

Appendix C

Evaporator

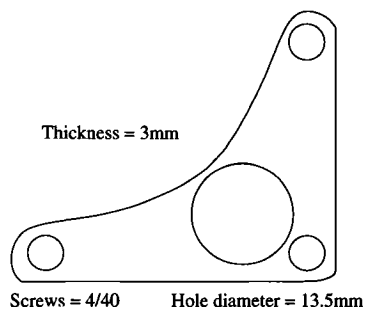


Figure C.1: Schematic design of the holder for the crucible.

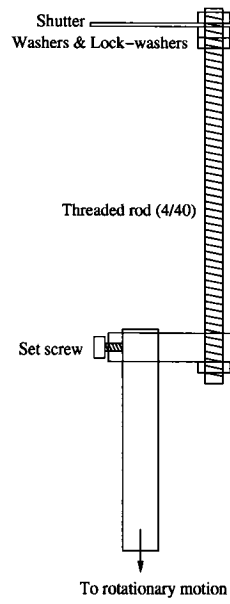


Figure C.2: Schematic design of the shutter.

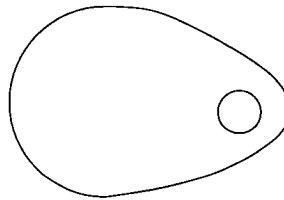


Figure C.3: Top view of the shutter plate.

Bibliography

- [1] D. Dowson, *History of Tribology* (Longman Inc., New York, 1979).
- [2] Oxford English Dictionary, www.oed.com.
- [3] B. Bhushan, *Handbook of micro/nano tribology*, 2nd ed. (CRC Press, Boca Raton, FL, 1999).
- [4] E. Meyer, H. J. Hug, and R. Bennewitz, *Scanning probe microscopy: the lab on a tip* (Springer, Berlin, 2004).
- [5] K. Oura *et al.*, *Surface science: an introduction* (Springer-Verlag, Berlin, 2003).
- [6] A. Czanderna, C. J. Powell, and M. T.E., *Specimen handling, preparation, and treatments in surface characterization* (Kluwer Academic / Plenum Publishers, New York, 1998).
- [7] J. F. O'Hanlon, *A user's guide to vacuum technology* (John Wiley & Sons, Hoboken, N.J, 2003).
- [8] H. Lüth, *Solid surfaces, interfaces and thin films* (Springer-Verlag, Berlin, 2001).
- [9] D. Woodruff and T. Delchar, *Modern techniques of surface science* (Cambridge University Press, Cambridge, UK, 1994).
- [10] J. Hudson, *Surface science: an introduction* (Butterworth-Heinemann, Stoneham, MA, 1992).

- [11] L. E. Davis, N. C. MacDonald, P. W. Palmberg, and G. Riach, *Handbook of Auger electron spectroscopy : a reference book of standard data for identification and interpretation of Auger electron spectroscopy data* (Physical Electronics Industries, Eden Prairie, Mn, 1976).
- [12] D. E. Gray, *American Institute of Physics Handbook*, 3rd ed. (AIP, New York, 1972).
- [13] F. Battye, G. Liesegang, R. Leckey, and J. Jenkin, *Phys. Rev. B* **13**, 2646 (1976).
- [14] P. Grutter, D. Rugar, and M. H.J., *Springer Series in Surface Science* (Springer-Verlag, Berlin, 1996), Vol. 28.
- [15] Omicron Vakuumphysik GmbH, D-6204 Taunusstein 4, Germany.
- [16] L. Howald *et al.*, *Appl. Phys. Lett.* **63**, 117 (1993).
- [17] MaTecK GmbH, <http://www.mateck.de/MeSiCrys/e07e.asp>.
- [18] W. Pearson, *Handbook of lattice spacings and structures of metals and alloys* (Pergamon, London, 1958).
- [19] I. Mauch, G. Kaindl, and A. Bauer, *Surface Science* **522**, 27 (2003).
- [20] Z. Zou, Z. Dong, A. Trifonov, and H. Nejo, *Journal of Vacuum Science & Technology B (Microelectronics and Nanometer Structures)* **20**, 1567 (2002).
- [21] Kurt J. Lesker Company, <http://www.lesker.com>.
- [22] Kimball Physics Inc., <http://www.kimphys.com>.
- [23] J. A. Venables, *Introduction to surface and thin film processes* (Cambridge University Press, Cambridge, 2000).
- [24] W. Liu and M. Santos, *Thin films: heteroepitaxial systems* (World Scientific, Singapore, 1999).

- [25] M. Tringides, *Surface diffusion: atomistic and collective processes* (Plenum Press, New York, 1997).
- [26] D. King and D. Woodruff, *The chemical physics of solid surface: growth and properties of ultrathin epitaxial layers* (Elsevier, Amsterdam, 2004), Vol. 8.
- [27] R. Bennewitz *et al.*, *Surface and interface analysis* **27**, 462 (1999).
- [28] R. Bennewitz *et al.*, *Surface Science* **438**, 289 (1999).
- [29] K. Glöckler, M. Sokolowski, A. Soukopp, and E. Umbach, *Phys. Rev. B* **54**, 7705 (1996).
- [30] S. Fösch, U. Barjenbruch, and M. Henzler, *Thin Solid Films* **172**, 123 (1989).
- [31] M. Kiguchi *et al.*, *Phys. Rev. B* **66**, 155424 (2002).
- [32] M. Yang and C. Flynn, *Phys. Rev. B* **41**, 8500 (2001).
- [33] R. Bennewitz *et al.*, *Phys. Rev. B* **62**, 2074 (2000).
- [34] L. Vitos, H. Skriver, and J. Kollar, *Surface Science* **425**, 212 (1999).
- [35] R. Smoluchowski, *Phys. Rev.* **60**, 661 (1941).
- [36] D. Farias *et al.*, *Surface Science* **420**, L93 (2000).
- [37] W. Hebenstreit *et al.*, *Phys. Rev. Lett.* **85**, 5376 (2000).
- [38] S. Fölsch *et al.*, *Surface Science* **497**, 113 (2002).
- [39] J. Repp, S. Fösch, G. Meyer, and K.-H. Rieder, *Phys. Rev. Lett.* **86**, 252 (2001).
- [40] W. Hebenstreit *et al.*, *Surface Science* **424**, L321 (1999).
- [41] R. Bennewitz, E. Gnecco, T. Gyalog, and E. Meyer, *Tribology Letters* **10**, 51 (2001).
- [42] A. Socoliuc, R. Bennewitz, E. Gnecco, and E. Meyer, *Phys. Rev. Lett.* **45**, 134301 (2004).

- [43] C. Mate, M. G., R. Erlandsson, and S. Chiang, *Phys. Rev. Lett.* **59**, 1942 (1987).
- [44] D. Tománek, W. Zhong, and H. Thomas, *Europhys. Lett.* **59**, 887 (1991).
- [45] F. Gao *et al.*, *Tribology Letters* **12**, 99 (2003).
- [46] F. Gao, P. V. Kotvis, and W. Tysoe, *Tribology Letters* **15**, 327 (2003).
- [47] F. Gao, P. V. Kotvis, and W. Tysoe, *Wear* **256**, 1005 (2004).
- [48] E. Gnecco *et al.*, *Phys. Rev. Lett.* **84**, 1172 (2000).
- [49] Y. Sang, M. Dubé, and M. Grant, *Phys. Rev. Lett.* **87**, 174301 (2001).